Chem Soc Rev

Nanoscale optical imaging in chemistry

Journal:	*Chemical Society Reviews*
Manuscript ID	CS-SYN-04-2020-000338.R3
Article Type:	Review Article
Date Submitted by the Author:	10-Jul-2020
Complete List of Authors:	Wilson, Andrew; University of Illinois at Urbana-Champaign, Chemistry Devasia, Dinumol; University of Illinois at Urbana-Champaign, Chemistry Jain, Prashant; University of Illinois at Urbana-Champaign, Department of Chemistry

Nanoscale Optical Imaging in Chemistry

*Andrew J. Wilson[1], Dinumol Devasia[1], and Prashant K. Jain[1,2,3,4]**

[1]Department of Chemistry, University of Illinois at Urbana-Champaign, Urbana, IL, 61801, United States

[2]Department of Physics, University of Illinois at Urbana-Champaign, Urbana, IL, 61801, United States

[3]Materials Research Lab, University of Illinois at Urbana-Champaign, Urbana, IL, 61801, United States

[4]Beckman Institute for Advanced Science and Technology, University of Illinois at Urbana-Champaign, Urbana, IL, 61801, United States

*Corresponding Author E-mail: jain@illinois.edu

Abstract

Single-molecule-level measurements are bringing about a revolution in our understanding of chemical and biochemical processes. Conventional measurements are performed on large ensembles of molecules. Such ensemble-averaged measurements mask molecular-level dynamics and static and dynamic fluctuations in reactivity, which are vital to a holistic understanding of chemical reactions. Watching reactions on the single-molecule level provides access to this otherwise hidden information. Sub-diffraction-limited spatial resolution fluorescence imaging methods, which have been successful in the field of biophysics, have been applied to study chemical processes on single-nanoparticle and single-molecule levels, bringing us new mechanistic insights into physiochemical processes. However, the scope of chemical processes that can be studied using fluorescence imaging is considerably limited; the chemical reaction has to be designed such that it involves fluorophores or fluorogenic probes. In this article, we review optical imaging modalities alternative to fluorescence imaging, which expand greatly the range of chemical processes that can be probed with nanoscale or even single-molecule resolution. First, we show that the luminosity, wavelength, and intermittency of solid-state photoluminescence (PL) can be used to probe chemical transformations on the single-nanoparticle-level. Next, we highlight case studies where localized surface plasmon resonance (LSPR) scattering is used for tracking solid-state, interfacial, and near-field-driven chemical reactions occurring in individual nanoscale locations. Third, we explore the utility of surface- and tip-enhanced Raman scattering to monitor individual bond-dissociation and bond-formation events occurring locally in chemical reactions on surfaces. Each example has yielded some new understanding about molecular mechanisms or location-to-location heterogeneity in chemical activity. The review finishes with new and

complementary tools that are expected to further enhance the scope of knowledge attainable through nanometer-scale resolution chemical imaging.

1. Introduction

Despite the availability of mechanistic models for many chemical reactions, many complex chemical processes, especially those that involve multiple spatiotemporally correlated steps, or those that take place in complex media, on surfaces, or those involving heterogeneous catalysis are not understood fully at the molecular level. Instead of reliance on indirect deductions from bulk-level kinetic measurements, it would be much more powerful to watch these processes directly on the molecular level. Such molecular-level probing would greatly advance our understanding of chemistry and lead to new discoveries in molecular dynamics, non-equilibrium statistical mechanics, surface science, and catalysis. This knowledge also serves a utilitarian purpose: it can be exploited for the optimization of reaction outcomes, yields, and performance, which is often at the heart of solutions to wide-ranging problems in energy conversion and storage, information storage and communications, water purification, and drug development. Conventionally, reaction performance, thermochemical properties, kinetics, and reaction mechanisms are measured and optimized on the bulk scale at which the chemical system consists of a large collection (ensemble) of molecules. The measurements, which are effectively averages over the entire ensemble, provide general insights and trends about chemical reactivity; but information about the precise reactivity of individual molecules is lost in the ensemble-averaging process because individual molecules in the ensemble are likely to be at different chemical states at any given time in the course of a chemical reaction. This stochastic heterogeneity is further exacerbated, especially in complex media, on surfaces, or in catalytic processes, by extrinsic heterogeneity that results from the different environments or adsorbate states of individual molecules. In addition to these sources of variability, surface reactions and heterogeneous catalytic processes also involve structural heterogeneities that result from differences in the local structures

and properties of active sites. Chemical measurements on the level of single nanoparticles (NPs), single sites, or single molecules reduce and ultimately eliminate the loss of valuable molecular information resulting from averaging over a large heterogeneous ensemble. Therefore, such measurements are able to elucidate much more precisely how local, nanoscale structures and environments influence chemistry and reveal chemical dynamics and structure-reactivity relationships that are often hidden in complex systems.

Far-field optical imaging offers a powerful platform for single-molecule, single-site, or nanometer-scale-resolution studies of chemical processes. This capability is the product of several factors: sensitivity of optical phenomena to molecular structure, suitability for in-situ measurements, compatibility with varied reaction media and environments, use of non-destructive or minimally destructive visible light radiation, and nanoscale spatial resolution that is now conventionally available[1,2] despite the conventional diffraction limit of optical imaging. The 2014 Nobel prize awarded for super-resolution fluorescence imaging highlighted the importance and power of optical imaging for the study of chemical behavior with nanoscale spatial resolution.[3] Today, fluorescence imaging and spectroscopy are routinely applied to study chemical processes at the molecular level in a vast array of complex biological systems, including in live cells and cell organelles. More recently, fluorescence imaging has been extended to report on molecular events in materials chemistry and catalysis. There are two basic strategies for the use of fluorescence imaging for monitoring chemical processes with sub-diffraction-limited spatial resolution: i) individual fluorescent molecules involved in the process are spatially localized by their stochastic, intermittent emission, which allows the process to be mapped with nanometer-scale resolution or ii) an external stimulus is used to trigger the interconversion of a probe molecule between a fluorescent and non-fluorescent form. A burst/loss of localized fluorescence serves as a signature

of an individual conversion event. These strategies have allowed chemical reactivity of several model reactions to be measured at the single NP and single molecule levels, as discussed in comprehensive reviews in recent literature.[4–9] However, an inherent limitation of fluorescence imaging is that only fluorogenic reactions or molecules modified with a fluorescent label can be interrogated, severely restricting the scope of chemical reactions that can be studied. In addition, one has to know in advance the species involved in the reaction. Therefore, there has been a need for fluorescent-label-free approaches that can be used in a much more general fashion for imaging chemical reactions.[10,11]

In this article we describe optical strategies that can be used to image a wide range of chemical reactions with a spatial resolution that extends down to individual NPs or individual molecules. It is noted that several other forms of microscopies have also been employed for probing chemical reactions with nanoscale spatial resolution. These include scanning electrochemical probe microscopies[12] (e.g., scanning electrochemical microscopy[13,14] and scanning electrochemical cell microscopy[15]), X-ray microscopy,[16,17] infrared nanospectroscopy,[18,19] scanning tunneling microscopy,[20] in situ transmission electron microscopy,[21,22] and multimodal combinations of these methods. Here, however, we focus on studies that make use of visible-range optical microscopy and spectroscopy. Our prime motivation is to highlight the progress made in the supplanting of fluorescence imaging and the alternatives now available for the optical probing of a broad range of chemical reactions. We have identified three specific types of optical imaging modalities that are alternative to molecular fluorescence and suitable for interrogating nanoscale chemistry: 1) NP PL, 2) localized surface plasmon resonance (LSPR) scattering, and 3) surface- and tip-enhanced Raman scattering. For each modality, we briefly describe the optical phenomenon, its key characteristics, and the practical methodology for typical measurements. Then, we review several

experimental case studies where the modality has been successfully implemented for obtaining new nanoscale insight into a chemical process that is otherwise unattainable from ensemble measurements. Each section concludes with the limitations of the imaging modality. Finally, we offer future directions in optical imaging that are expected to enrich our understanding of chemistry on the nanoscale.

2. Nanoparticle photoluminescence

PL is broadly defined as light emission from matter following a light absorption event. Advances in the synthesis of nanostructured materials have provided a large library of photoluminescent NPs with a range of tunable emission properties. A cornerstone property, PL brilliance, has been engineered to enable routine optical detection of select solid-state materials, especially high-quality semiconductors, at the single NP level. In some cases, the brilliance is strong enough that the full PL spectrum of a single NP is measurable. At the single-NP level, it has also been observed that PL may not be steady; it can show an intermittent or on/off blinking behavior, as is the case for semiconductor nanocrystals.[23,24] These PL characteristics: brilliance, the emission wavelength maximum of the spectrum, and intermittency inherently depend on the NP structure, composition, size, and local environment. In the event that a chemical reaction alters the properties of a photoluminescent NP, its characteristic PL brilliance, emission wavelength, and/or nature of intermittency may change (Figure 1). Although the bulk PL of an ensemble of NPs can be used to track a chemical reaction, as shown in Figure 1a, c, the information can be rather limited or even misleading. At any time in the course of a chemical reaction, individual NPs are likely to be at different stages; the bulk PL provides an average picture of this heterogeneous ensemble. The time-evolution of the bulk PL is not in such a case truly representative of the time-evolution of

chemical and structural changes occurring at the NP level. This is why single-NP-level PL can be powerful for probing of chemical transformations on the nanoscale. Single-NP-level PL does not suffer from the limitation of NP-to-NP heterogeneity. In-situ monitoring of the single-NP-level PL in the course of a reaction allows the structural changes in the NP to be tracked in time.

The physiochemical sensitivity and brilliance of PL make it simple to implement single-NP-level PL for probing chemical reactions on the nanoscale in a wide range of chemical environments. In a typical experiment, photoluminescent NPs are sparsely dispersed over a supporting substrate or embedded within a condensed phase matrix. The NP-loaded substrate is mounted in an optical microscope. Incident light (typically from a laser) is focused using a microscope objective onto a single NP (or a small field of NPs). The ensuing PL is collected through the same objective and directed onto a CCD camera, a spectrograph, or a photon counting detector, e.g., photomultiplier tube (PMT) or an avalanche photodiode (APD). Continuous measurement of the PL intensity, spectrum, and intermittency from a single NP allows chemical processes occurring on the NP to be probed in real time. The chemical process may be a solid-state transformation of the NP itself or it may be a chemical reaction taking place on the surface or in the vicinity of the NP. The PL is a direct probe in the former case and an indirect one in the latter. In the following section, we review several examples in which the nanoscale-resolution measurement of chemical processes has been enabled by single-NP PL imaging and spectroscopy. The examples are classified by two different types of NPs with distinct PL mechanisms: semiconductor NPs and noble metal NPs. For each class, the chemical processes that are possible to be tracked are described. The general limitations of NP PL for the study of chemical reactions are discussed at the end of this section.

2.1 Semiconductor nanoparticles

In a semiconductor NP (e.g., a quantum dot), light of photon energy greater than energy gap between the valence and conduction bands is absorbed. The light absorption results in the excitation of an electron from the valence to the conduction band forming a charge-separated or a bound electron–hole pair. Excited charge carrier relaxation followed by radiative recombination of the electron-hole pair results in the emission of light typically with a photon energy lower than the excitation energy. If a fraction of the excited charge carriers returns to the ground state by non-radiative means, the emission quantum yield decreases. One form of such non-radiative loss is the transfer of the energetic charge carrier from the semiconductor NP to an acceptor. Such a charge transfer event is detected by a loss or decrease of the PL brilliance. Amirav and Alivisatos used this concept to probe charge transfer and the Pt-catalyzed H_2 evolution reaction at the single-NP level.[25] Specifically, the researchers measured PL from a single Pt-tipped CdSe quantum dot embedded in a CdS quantum rod nanostructure. Visible light absorbed by this quantum system excites electrons into the conduction band. The excited electrons either recombine with the holes in the valence band and emit light or transfer to the Pt tip. Electrons trapped by the Pt tip either non-radiatively recombine on a slower timescale with holes confined in the semiconductor or participate in H_2 evolution (if the surrounding medium contains H^+). In the charge-separated state, the PL intensity is quenched due to the prevalence of Auger relaxation of newly produced e^-–h^+ pairs in the semiconductor. The single-NP PL intensity thus serves as a relative measure of the prevalence of the charge-separated state. From the measured single-NP-level PL intensity plotted as a function of the excitation intensity, the researchers were able to infer the lifetime of the charge-separated state and also identify features that signify the consumption of photogenerated holes confined within the semiconductor and the consumption of Pt-trapped electrons by the H_2

evolution reaction. Any changes in the kinetics of these processes, say resulting from a modification of the reaction medium, were directly reflected in the single-NP PL trends. The light intensity-dependent trend of the single-NP PL also varied from one NP to another. This heterogeneity resulted from structural differences between individual nanostructures, particularly in terms of the quantum dot and rod dimensions. From an analysis of PL trends from several individual nanostructures, the researchers were able to determine the effect of these geometrical parameters on the relative rates of electron and hole consumption and identify the structural dimensions at which the various charge transfer/consumption rates are optimal for photocatalytic H_2 production. This level of insight was unattainable from prior bulk-level photocatalytic H_2

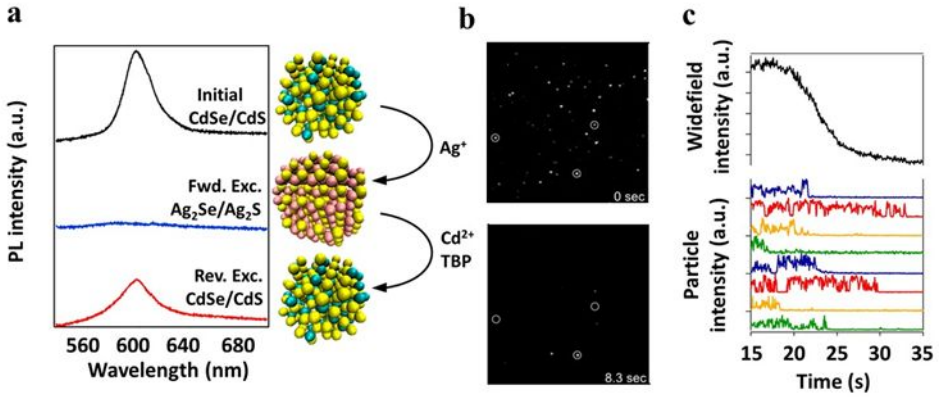

Figure 1. Imaging the chemical transformation of a single semiconductor NC. (a) (Left) The PL of CdSe/CdS NCs (black curve) is lost upon exchange with Ag^+ (blue curve). By subsequent exchange of the Ag_2Se/Ag_2S NCs thus formed with Cd^{2+}, the PL is recovered (red curve). The recovered PL has a similar spectrum as the original PL. (Right) A cartoon showing the forward and reverse cation exchange between Cd^{2+} and Ag^+ in a Se/S anionic framework. Reprinted with permission from ref 29. Copyright 2015 American Chemical Society. (b) A wide-field PL image of several isolated single CdSe/CdS NCs (labeled by white circles) under 457 nm laser excitation as they undergo cation exchange conversion to Ag_2Se NCs. Bright PL is observed for all NCs at t = 0 s, while at t = 8.3 s, a majority of NCs have lost their PL due to a conversion to non-emissive Ag_2Se NCs. (c) Time-trajectories of PL intensity during cation exchange for individual NCs (colored curves) show a sharp transition. The ensemble-averaged trajectory (black curve) on the other hand gives the appearance of a gradual conversion. Reprinted with permission from ref 27. Copyright 2014 American Chemical Society.

production measurements, which underscores the power of single-NP-level measurements for enhancing understanding of photocatalysis.

Because of the dependence of semiconductor PL on a NP's inherent attributes such as its geometry, composition, crystallographic, and electronic structure, physical and chemical transformations of a semiconductor can be followed at the single-NP-level by measurement of the features of light emission from a NP. One solid-state transformation that has been studied in this manner is ion-exchange in semiconductors. Ion exchange involves the replacement of the native cations (or anions) of an ionic crystal by foreign cations (or anions).[26] There are cases, especially with nanocrystals (NCs), where the entire sub-lattice is replaced and an ionic crystal of a different composition is obtained. It had been unclear how this dramatic transformation takes place at the atomic level. What is the mechanism by which all the ions are place exchanged? To obtain such insights, Jain and coworkers watched the ion exchange transformation of a single semiconductor NC by using the composition-sensitive PL of the NC as a probe (Figure 1).[27] The single-NC resolution of the study ensured that the measured kinetics of the exchange reaction was not convoluted by averaging of the response of many NCs. The researchers performed in-situ PL imaging (50 ms time resolution) of luminescent CdSe/CdS NCs (~4 nm diameter) undergoing conversion to non-luminescent Ag_2Se/Ag_2S NCs (Figure 1) in a medium containing Ag^+. CdSe/CdS NCs were immobilized inside a microfluidic flow cell with a low enough area density so that the NCs were spatially isolated from one another and multiple individual emitters could be distinguished in the microscope field of view. The PL intensity from each CdSe/CdS NC was measured in the course of the exchange of Cd^{2+} by Ag^+ to form a Ag_2Se/Ag_2S NC. Bright PL was observed from emissive CdSe/CdS NCs at time t = 0 s (before cation exchange) while only a small fraction emitted light at t = 8.3 s, indicating a majority had converted to Ag_2Se/Ag_2S. By t = 12.4

s all NCs had lost their PL indicating a full conversion of the entire field of view of NCs. The PL imaging captured a key observation: the PL of each NC did not gradually decrease until it was fully extinguished; rather individual NCs underwent a sudden transition from emissive to non-emissive. Over time, NCs in the field of view turned off one-by-one as they made this transition. This observation is clearly captured in time-trajectories of the PL intensity (Figure 1c). The averaged PL intensity from the ensemble of NCs shows a gradual decrease in time until it falls to zero. However, the time trajectory of each individual NP shows a rapid transition from a luminescent CdSe/CdS state to the non-luminescent Ag_2Se/Ag_2S state. This shows that the cation exchange transformation is a switch-like transition (occurring over a few 100 ms) of the entire NC from CdSe/CdS to Ag_2Se/Ag_2S rather than a gradual ion-by-ion replacement. The single-NC trajectories also reveal that the instant of time at which an individual NC makes a switch is unique and different from other NCs. This NC-to-NC heterogeneity in the onset time of the sudden reaction was determined to result primarily from stochastic kinetics rather than the result of a structural difference between the NCs. Due to the different switching times of individual NCs, the ensemble-averaged trajectory appears gradual. If one uses this ensemble-level information to make an inference about the kinetics of the process, it gives a false perception that the cation exchange transformation takes place via a sequence of individual, diffusion-limited ion exchange steps. In reality, the cation exchange of a NC is a co-operative phase transition,[28] as we learn from the kinetics measured directly on the single-NC-level and supported by simulations. This study highlights how rich mechanistic information that lays hidden in ensemble-level kinetic measurements can be uncovered by single-NC-level imaging.

In addition to emission intensity, PL intermittency or on-off blinking, is a characteristic trait of quantum-sized semiconductor NCs, i.e. quantum dots. Jain and coworkers showed that the on-off

PL blinking of a quantum dot can be used to monitor the dynamics of a chemical reaction.[29] The researchers monitored the time evolution of the PL blinking behavior of single NCs undergoing forward and reverse cation exchange between CdSe/CdS (~6 nm diameter) and Ag_2Se/Ag_2S phases with 50 ms resolution. The fraction of emissive NPs to total NPs at any given instant was used as a measure of the relative prevalence of the on-state to the off-state. It was found in the forward exchange that the blinking dynamics of a CdSe/CdS NC changes right before the sharp transition to the Ag_2Se/Ag_2S phase. In particular, the off-state becomes more prevalent as the transition point is approached. In the reverse transformation, right after the sharp transition to the CdSe/CdS phase, the NC has a much a higher prevalence of the off-state. The prevalence of the off-state decreases until the blinking dynamics becomes steady at long times after the transition point. From this observed behavior, it was inferred that the forward cation exchange reaction is preceded by the interstitial doping of the CdSe/CdS NC with Ag^+. These interstitial dopants and associated lattice vacancies serve as sites for non-radiative recombination and increase the prevalence of the NC to be non-emissive (off). This doped, defective CdSe/CdS NC, which is a precursor to the co-operative cation exchange transformation, was thus captured by monitoring the blinking behavior. Analogously, in the reverse reaction, the CdSe/CdS NC formed right after the co-operative transition is defective due to the presence of remnant Ag dopants and/or Cd vacancies. As a result, the NC has a higher prevalence of the non-emissive state, i.e., the NC has a lower emission quality. These Ag dopants and Cd vacancies are purified from the CdSe/CdS NC over a longer timescale, which was found to be several-few 10s of seconds as compared to the few 100 ms timescale of the co-operative transition. During this purification stage, the off-state becomes less prevalent, i.e., the emission quality improves, until it reaches stability. Thus, imaging of the PL blinking dynamics of single semiconductor NCs revealed precursor doping and post-transition

purification stages in the solid-state transformation and allowed the determination of timescales of these processes. This study highlights the mechanistic richness of chemical information contained within the PL properties of a NC.

2.2 Noble metal nanoparticles

In NPs of noble metals, especially Au, optical illumination can generate electron-hole pairs either via direct photoexcitation of d-to-sp band electronic transitions, i.e., interband transitions, or through the excitation and subsequent decay of LSPRs. An LSPR is a coherent, collective oscillation of conduction band electrons induced by the oscillating electric field of incident light and confined by the boundaries of the NP. An LSPR decays either through radiative scattering or through the generation of electron-hole pairs in the metal. Electron-hole pairs can then radiatively recombine to give broad, visible-range PL[30] or they may interconvert to LSPRs leading to light emission or scattering centered at the LSPR frequency (Figure 2a).[31–33] While radiative electron-hole recombination is inefficient in bulk noble metals due to the high density of states and fast non-radiative relaxation, in NPs, the radiative recombination rate is significantly enhanced by the near-field generated by the LSPR through a Purcell-like effect.[34] The resulting enhancement of the PL brilliance makes single NP-level measurements feasible.[34,35]

Majima and coworkers pioneered the use of PL of Au NPs as a reporter of local photochemical reactions,[32,33,36–38] as described in their seminal paper.[32] The researchers had found from a bulk study that Pt-modified Au nanorods are effective photocatalysts for H_2 generation; the Au nanorod serves as the light absorber and the coated Pt NPs serve as co-catalysts for H_2 generation. The researchers used 405 nm light to excite the interband transitions in spatially isolated Pt-modified Au nanorods. The resulting emission from the nanostructures was imaged. The images showing

individual emitters were spatially correlated with transmission electron microscopy (TEM) images, which identify the morphology of the individual nanostructures. Individual Pt-modified Au nanorods showed much lower emission intensities as compared to individual Au nanorods. Furthermore, a NP-by-NP analysis showed that the PL emission intensity depended on the location and coverage of the Pt, which varied considerably from one nanostructure to another. Nanorods with Pt on the tips showed considerably quenched PL compared to unmodified Au nanorods. Nanorods that were also covered with Pt at the lateral surfaces had even lower PL emission, while nanorods with surfaces fully coated with Pt showed no detectable emission. The quenching of emission in Pt-modified nanorods suggested that photoexcited electrons generated in the Au were transferred to the Pt. In an aqueous medium, these electrons are consumed for the reduction of H^+ to H_2 and the holes left behind in the Au are filled by electrons from the oxidation of methanol. Although the single-NP studies appear to be conducted under non-photocatalytic conditions, the electrons transferred to the Pt nevertheless were unavailable for radiative processes. The resulting emission quenching therefore served as a probe of the electron transfer. The quenching efficiency, which can be seen as a metric of the electron transfer rate, was found to depend on the coverage and spatial locations of the Pt NPs and the diameters of the Au nanorods. Thus, the single-NP-level study provides more detailed understanding of structure-activity relationships in bimetallic NP photocatalysts.

Single-NP-level emission quenching measurements have since been extended to other bimetallic NP systems for insights into photocatalytic reactions such as H_2 evolution on Pt-coated Au NPs,[32,33] formic acid dehydrogenation on Pd-coated Au NPs,[36] and ethanol oxidation on Au NPs.[37] In a more recent application, PL was used for in situ monitoring of the etching of Au triangular nanoprisms, a process used for the synthesis of NP photocatalysts with a diversity of geometries

(Figure 2b,c).[38] The oxidative etching process modifies the NP morphology, which determines in part the resonant frequency of the plasmonic emission channel and the corresponding spectrum. By monitoring the measured emission intensity and the spectrum, the etching of a nanoprism was tracked in real time. From the measured changes in the emission spectra and resonant frequencies (Figure 2c), changes occurring in the size and shape of each nanoprism as it undergoes etching were determined.

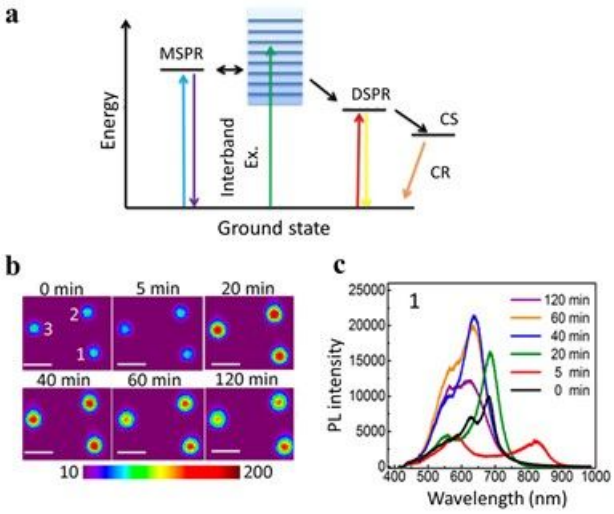

Figure 2. PL imaging of single noble metal NPs. (a) Energy diagram showing a proposed mechanism of PL from a Au triangular nanoprism following an interband electronic excitation. Interband excitation of Au leads to the generation of electron-hole pairs that decay by excitation of a dipolar or multipolar LSPR, labeled DSPR and MSPR, which can further decay radiatively leading to the emission of light. The transfer of the excited electron to an acceptor generates a charge separated state (CS), quenching the emission and opening an alternate charge recombination (CR) pathway. Reprinted with permission from ref 33. Copyright 2016 American Chemical Society. (b) Emission images and (c) emission spectra of single Au nanoprisms at various time-points in the course of their oxidative etching. The individual-nanoprism-level changes in the emission intensity and spectral features reflect the structural changes that accompany the etching reaction. Reprinted with permission from ref 38. Copyright 2017 American Chemical Society.

By in-situ monitoring of the changes in the PL of semiconductor and noble metal NPs, chemical processes can be probed on the nanoscale. PL measurements from single NPs or reduced ensemble

sizes often provide insight into chemical behavior and trends that are otherwise hidden in traditional ensemble-averaged measurements conducted on heterogeneous systems. As discussed by specific examples, PL intensity, intermittency, and spectral characteristics serve as chemically informative probes in an array of conditions and environments. The broadening list of nanoscale physiochemical processes unlocked by single-NP PL now includes surface charge trapping[39] and crystal facet-dependent charge accumulation dynamics[40] in photocatalysts. However, solid-state PL has intrinsic limitations for nanoscale probing of chemical reactions. By its very nature, light emission is preceded by the generation of electron-hole pairs or excitons. Often in the presence of interfacial redox and solid-state chemical reactions, the lifetime and dynamics of carriers change resulting in a modification of the PL properties. But often these changes are convoluted with those caused by any accompanying changes in the NP morphology. This convolution makes it difficult to extract information about charge carrier-driven chemical events from PL. Further, there is a fundamental limit to the spatial resolution: even though the diffraction limit does not dictate the resolution when NPs are individually addressable, the resolution is fundamentally limited by the NP size, which defines the region from which the emission emanates. Finally, the optical information is electronic, and thus quite unlike vibrational absorption or scattering, it is not a reporter of bond-breaking and bond-formation steps, unless there is *a priori* knowledge of these elementary steps in a given reaction.

3. Localized surface plasmon resonance scattering

As described in the previous section, LSPRs represent a characteristic interaction of the conduction band electrons of a noble metal NP with light. LSPR frequencies depend on the NP morphology or configuration, NP composition (dielectric function), and the composition

(dielectric function) of the surrounding environment. Following their excitation, LSPRs relax either radiatively, which results in light scattering centered at the resonant frequency, or they non-radiatively decay into electron-hole pairs.[41] The radiative channel is highly efficient in NPs of 10s of nm diameters. NP scattering cross-sections far surpass their physical size,[42] which enables routine optical detection of single NPs with broadband light excitation. For NPs of the coinage metals, Ag, Au, and Cu, the LSPR frequencies are in the visible region of the electromagnetic spectrum, making these NPs suitable for optical microscopy. Moreover, the large scattering cross-section and the sensitivity of LSPR frequencies and cross-sections to NP and environmental characteristics make LSPR scattering a capable single NP-level probe of chemical reactions. The morphological and compositional sensitivity of LSPRs permits solid-state and interfacial chemistry to be monitored at the single-NP level; the sensitivity to the local environment allows surface adsorbate and solution-phase chemical reactions occurring within the range of the plasmonic near-field to be monitored.

A common approach used for the measurement of the LSPR scattering and spectrum of a single noble metal NP is dark-field scattering microscopy. In this technique, a substrate, e.g., a glass cover slip is sparsely decorated with NPs and is mounted in an optical microscope and illuminated with the help of a condenser by a focused, high-incidence-angle annulus of white light. The white light illumination excites visible-range LSPRs, resulting in LSPR scattering. An objective of a numerical aperture lower than that of a condenser collects low-angle light scattered by individual NPs; high-incidence-angle excitation light is rejected. The collected scattered light is detected by a charge-coupled device (CCD) camera to produce an image of bright scattering from individual NPs against a dark background (Figure 3a). The dispersion of the collected light using a slit-equipped spectrometer placed in the detection path allows a scattering spectrum to be obtained

from single NPs. The simplicity of dark-field scattering microscopy measurements, coupled with the single-NP-level sensitivity of LSPR scattering, make LSPR spectroscopy a powerful platform for studying chemistry on the nanoscale. In the following section, we highlight examples where the LSPR scattering of individual NPs is used as a reporter of local chemical reactions. First, we explore how the morphological and compositional sensitivities of single NP LSPRs have been exploited for monitoring galvanic and interfacial electrolytic redox processes. Next, we showcase studies wherein the local environmental sensitivity of LSPRs is exploited for tracking surface and solution-phase chemical processes on the nanoscale. We conclude the section by discussing advantages and limitations of LSPR scattering for nanoscale studies of chemical processes.

3.1 Redox processes that involve the plasmonic nanoparticle

Galvanic reactions

Galvanic replacement is the spontaneous exchange of phase between two metals with different reduction potentials. When a solution of a metal ion with a more positive reduction potential is in contact with a metal of a more negative reduction potential, the latter is corroded and transferred into the solution phase in its cationic form, while the former is reduced to its zero-valent metallic form and transferred to the solid-state. A classic example is the galvanic corrosion of Ag in a solution containing Au^{3+}. In this reaction, Au^{3+} accept three electrons from three Ag atoms to form Au and three Ag^{+}. Jain and coworkers monitored this galvanic replacement reaction at the single-NP level by in-situ tracking of the LSPR scattering of a Ag NP (~40 nm diameter) under flow of a Au^{3+} solution.[43] The observed changes in the LSPR characteristics served as a reporter of the transformation of the NP. In the reaction, the composition of the NP changes from Ag to Au-rich and the morphology changes from quasi-spherical to nanocage-like, as shown by TEM imaging,

which complemented the LSPR scattering microscopy (Figure 3a, b). Au nanostructures have a lower scattering cross-section and a lower energy LSPR than Ag nanostructures. Thus, the galvanic exchange transformation of a NP is manifested in a decrease of its scattering intensity and a red-shift of the LSPR spectrum (Figures 3c). However, time trajectories of single-NP LSPR scattering intensity revealed a rapid switch from a strongly scattering state to a weakly scattering state. This switch was accompanied by a red-shift of the LSPR spectrum (Figure 3c). The researchers were able to infer that the galvanic exchange transformation of a NP from a Ag NP to a Au-rich nanocage is sudden and not gradual. Ex-situ electron microscopy and modeling of the solid-state kinetics showed that the galvanic replacement reaction involves a rate-limiting formation of atomic voids in the Ag lattice resulting from early exchange steps. Once a void of a critical size is formed, there is a rapid progression of the galvanic exchange reaction throughout the NP by the growth of the voids, limited only by mass transport. This mechanism is exhibited in the sudden onset of the galvanic exchange transformation observed in the single-NP trajectories. By contrast, the ensemble-averaged time trajectory obtained from many NPs showed a gradual decrease in the scattering intensity. This gradual evolution is not a reflection of the true solid-state kinetics of the galvanic process; this apparent evolution results from the phenomenon that each individual NP exhibits a finite waiting time before it makes a switch to the product phase. These waiting times are stochastically dispersed for the ensemble of NPs. Thus, the true nature of galvanic corrosion, which is obscured in ensemble measurements, is revealed by single-NP scattering measurements.

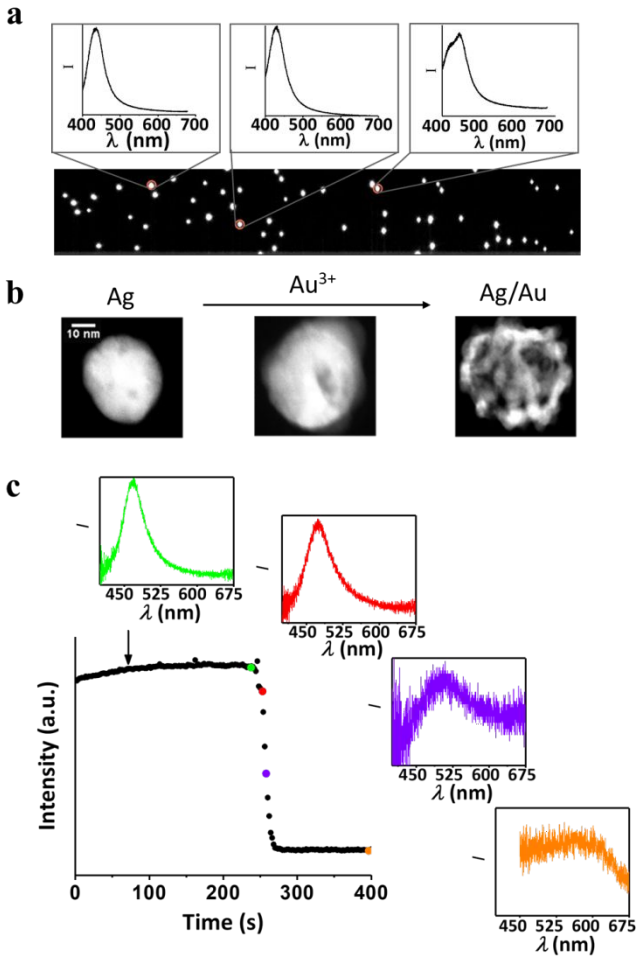

Figure 3. Imaging the galvanic exchange of single NPs. (a) Optical dark-field scattering image showing several isolated, individual Ag NPs. LSPR spectra of three chosen NPs from the wide-field image are also shown. (b) High-angle annular dark-field scanning tunneling electron microscopy images showing the structural progression in the galvanic exchange reaction from an unreacted Ag nanosphere to one that has undergone partial galvanic replacement by Au and eventually to a Au/Ag nanocage. (c) Time-trajectory of the LSPR scattering intensity of a single NP over the course of galvanic replacement of Ag with Au (black trace). The trajectory shows that the galvanic exchange occurs in the form of a sharp transition. Representative LSPR scattering spectra are shown at selected time-points along the trajectory: before the sharp transition (green), soon after the start of the transition (red), mid-point of the transition (purple), and well after the transition (orange). The decrease in intensity and red-shift in peak wavelength is characteristic of the addition of Au and a structural change in the NP. Reprinted with permission from ref 43. Copyright 2014 John Wiley and Sons.

This single-NP LSPR-based method has been used to study the influence of the ligand shell of a Ag NP (25–50 nm diameter) on the true kinetics of the galvanic transformation.[44] From single-

NP trajectories, it was found that with a ligand shell of a greater thickness, the typical waiting time before a NP makes a switch to the product phase is longer and the dispersion of waiting times across the population of NPs is wider. From these observations, it was inferred that alkanethiol surface ligands on Ag NPs pose an energy barrier for galvanic exchange. From an analysis of the NP-to-NP heterogeneity in the kinetics, the nature of the ligands was found to have a much stronger influence on the galvanic exchange kinetics than the NP size, shape, or crystallinity. In a follow-up study, the Jain group found from single NP (~40 nm diameter) trajectories that the mechanism of the galvanic replacement process can be completely overturned by solution-phase additives.[45] Typically, the galvanic transformation is a catastrophic process limited only by void nucleation; but in the presence of high concentrations of Cl^-, the transformation takes place via a sequence of atom-by-atom exchange steps, limited only by diffusion.

Song and coworkers found using single-NP LSPR scattering that temperature governs the mechanism of galvanic transformation of single Ag nanocubes to Au nanoboxes.[46] At room temperature, individual nanocubes undergoing a transformation to nanoboxes showed an abrupt red-shift in their LSPR frequency at an early state, following which the LSPR frequency reached a steady value. At an elevated temperature, the LSPR frequency undergoes an abrupt shift at an early stage, but at a later stage it shows fluctuations in time and considerable NP-to-NP heterogeneity. Moreover, the time-evolving LSPR scattering spectra showed complex multi-peaked shapes. These observations point to the development of complex morphologies at intermediate stages in the exchange reaction performed at higher temperatures. This insight is verified by ex-situ TEM imaging. TEM studies showed that the room temperature galvanic reaction produces nanocubes with granular, lumpy surfaces; on the other hand, the reaction at elevated temperatures produces nanocubes with smooth, even surfaces via complex intermediate

morphologies. The temperature-dependence of the mechanism of the galvanic exchange and the surface morphology of the product was attributed to the higher rate of interdiffusion between Au and Ag at an elevated temperature. Thus, in situ single-NP LSPR spectroscopy combined with other ex situ characterization provides a detailed look at how the kinetics of galvanic exchange controls the final nanoarchitecture of the product. Analogous insight has been obtained by Zhao and coworkers who employed in situ single-NP LSPR spectroscopy to interrogate the mechanism of galvanic exchange of $AuCu_3$ nanorods (35.5 nm length and 12.6 nm diameter) with Au^{3+}.[47] Depending on the kinetics of exchange, hollow AuCu nanorods or AuCu@Au core-shell

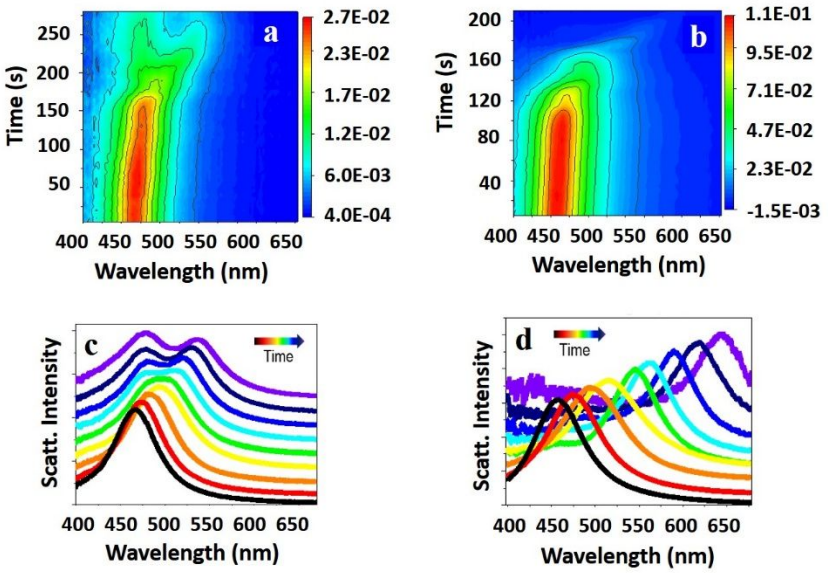

Figure 4. Formation of bimetallic NPs probed at the single-NP level by LSPR scattering spectroscopy. (a, b) Two representative examples of a color map showing the time evolution of the LSPR scattering spectrum of a single Ag NP as it undergoes a galvanic exchange reaction with $[PtCl_6]^{2-}$. The LSPR scattering intensity is represented by the color scheme provided in the legend. (c, d) Slices (scattering spectra) at select time points from the color maps shown in (a) and (b), respectively. Panel c shows an example where the LSPR band red-shifts with time and eventually splits into two bands. Panel d shows an example where the LSPR band undergoes a continuous red-shift with time. The diversity of spectral behavior emphasizes the importance of single NP measurements for studying the formation of complex nanostructures. Reprinted with permission from ref 48. Copyright 2016 John Wiley and Sons.

nanospheroids were formed. In the latter case, a unique intermediate nanostructure with a hollow junction and a dumbbell shape was captured in the single-NP spectral monitoring.

The examples of galvanic reactions discussed thus far involved an exchange between two plasmonic metals with LSPRs in the visible frequency region. However, with the use of white-light, dark-field microscopy for reaction monitoring, only one of the metals is required to have a visible-range LSPR in its NP form. The other metal need not be plasmonic. In this scenario, one can track an increase (decrease) in the LSPR scattering intensity as the plasmonic metal is reductively deposited onto the solid phase (oxidatively dissolved in the form of cations into the liquid phase). In a study by Jain and coworkers, single NP LSPR scattering was used to examine the formation of bimetallic NPs driven by galvanic replacement of Ag in spherical NPs (46 nm) with $[PtCl_6]^{2-}$.[48] Although scattering intensity trajectories of individual NPs followed a similar time evolution as the ensemble-averaged trajectory, the spectral evolution was variable across the population of NPs (Figure 4) and three different types of evolution were observed. While one class of NPs show a progressive red-shift in the LSPR frequency as the reaction progresses, another class exhibits an early stage of LSPR red-shift followed by a splitting of the LSPR peak into two bands. A third class shows LSPR red-shift at early stages followed by a blue-shift at late stages. Combining these observations with single-NP level polarization anisotropy of LSPR scattering, ex-situ TEM imaging, and discrete dipole approximation simulations, the researchers determined the mechanism of structural evolution in the galvanic exchange process: at early stages, there is anisotropic oxidation of Ag to AgCl along with the reductive deposition of Pt clusters on the NP surface. At later stages, the large lattice strain between the unreacted Ag and the overdeposited AgCl induces an extrusion of the Ag inclusions. This complex structural evolution leads to the formation of the multi-domain Ag/AgCl/Pt nanostructures observed in TEM images. Such detailed

understanding of a multi-component nanostructure formation is not conventionally available because it is obscured in ensemble-level kinetic studies, but it is valuable for the design of exquisite nanoarchitectures with targeted functionality.

Metal-catalyzed redox reactions

Another form of a redox reaction is one catalyzed by a metal NP. In these cases, the metal NP acts as a source and sink of electrons. In catalytic reactions, where the rate of the oxidation half-reaction is greater than the rate of the accompanying reduction half-reaction, the metal NPs are transiently charged with excess electrons. Mulvaney and coworkers used LSPR scattering for monitoring the charging-discharging cycle of individual Au NPs serving as catalysts for ascorbic acid oxidation.[49] The researchers exploited the fact that the LSPR frequency is a function of the square root of the free electron concentration of the metal NP; so when the NP gets charged with excess electrons, the LSPR frequency increases, i.e., shifts toward blue wavelengths. It was found that in the catalytic reaction studied in an aqueous medium, electrons are first injected from the ascorbic acid into a Au NP, as evidenced by a blue-shift of the LSPR. Subsequently, dissolved O_2 accepts the excess electrons and undergoes reduction to form water. The unloading of excess electrons resulted in a red-shift of the LSPR frequency back to its original value. Thus, elementary steps in the redox reaction were discerned by using the LSPR scattering as a reporter. The researchers were also able determine from the magnitude of the LSPR shift the loading density of excess electrons on a NP.

Electrochemical and photocatalytic reactions

In contrast to the galvanic and redox reactions described above, electrochemical reactions use an external source of electrical potential for driving a non-spontaneous reaction. Like galvanic

reactions, electrochemical reactions involving plasmonic nanostructures with visible-range LSPRs can routinely be monitored at the single-NP level. The monitoring of Au NP charging-discharging in a catalytic redox reaction was extended by the Mulvaney group in 2009 to an electrochemical process, where instead of reduction and oxidation half-reactions the application of potentials, induces charging-discharging of a NP.[50] Au NPs were attached onto an indium tin oxide (ITO) electrode. The LSPR scattering spectra of individual NPs were tracked as the electrode potential was varied (Figure 5a). As the potential was scanned toward more negative values, the LSPR frequency blue-shifted indicating a loading of excess electrons onto the NP. The effect was most pronounced for Au nanorods. When the potential was scanned back to positive values, the LSPR frequency red-shifted and returned to its original position. For a comprehensive study of charge transfer and storage processes occurring during such electrochemical cycling, Landes and coworkers developed a method for simultaneously measuring LSPR spectra from a population of individual Au NPs subjected to an applied electrochemical potential.[51] From the expected shift in the LSPR spectra, the researchers were able to probe charging of Au NPs, but they also observed in the large set of single-NP data varied spectral responses, including increases in the scattering intensity, broadening and loss of the Lorentzian lineshape of the LSPR band, and anomalous red-shifts in the LSPR frequency under cathodic potentials. These spectral responses were traced to reversible and irreversible chemical reactions that accompany and/or compete with the charging process. The prevalence of these distinct processes varied from NP to NP. This study highlights the power of higher throughput single-NP studies for discerning unanticipated chemical processes that take place in metal NP electrochemistry. These diverse processes would not have otherwise been resolved in an ensemble measurement or a smaller set of single-NP measurements.

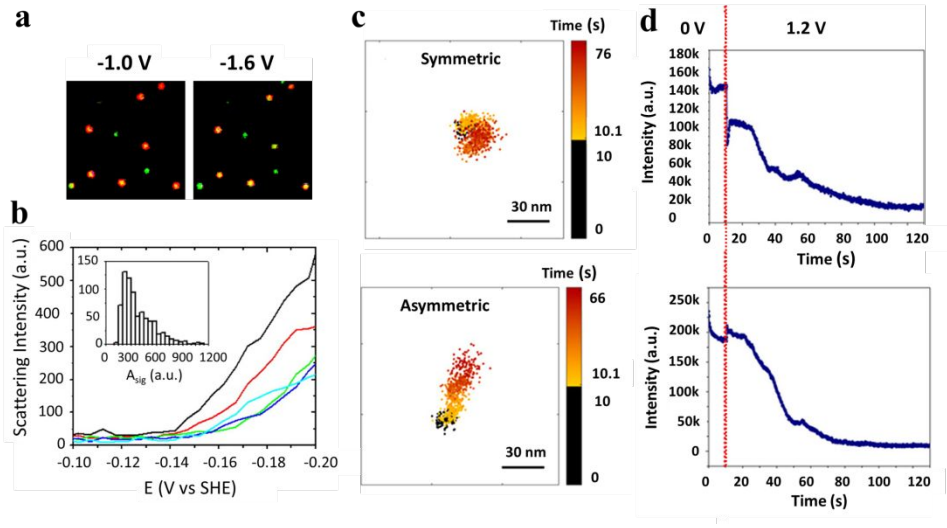

Figure 5. Electrochemical reactions on single NPs. (a) Color images of LSPR scattering of Au NPs showing individual nanorods (red) and individual nanospheres or trigonal nanoprisms (green) at applied potentials of -1.0 V and -1.6 V. When the potential is made more negative, the Au nanorods became charged with excess electrons, as indicated by the LSPR scattering color changing from red at -1.0 V to yellow-orange at -1.6 V. Reprinted with permission from ref 50. Copyright 2009 American Chemical Society. (b) LSPR scattering intensity as a function of applied potential, showing the electrochemical deposition and growth of individual Ag NPs on a transparent substrate electrode. Inset shows a distribution of the scattering intensity from individual electrochemically synthesized Ag NPs. Reprinted with permission from ref 52. Copyright 2013 American Chemical Society. (c) Scatter plots showing the (x,y) center locations of LSPR scattering from a single Ag NP for the first 10 s during which the potential was 0 V (black dots) and for the time period after 10 s during which an oxidizing potential of 1.2 V was applied (orange to red dots). The top example shows a symmetrically oxidizing Ag NP and the bottom example shows asymmetric oxidation of a NP. (d) Time-trajectories of the scattering intensity corresponding to the plots in (c). The vertical dotted red line denotes the time at which the applied potential was stepped from 0 to 1.2 V. Reprinted with permission from ref 53. Copyright 2018 American Chemical Society.

Another class of electrochemical reactions where single-NP-level LSPR monitoring has proven useful is the electrochemically-driven formation and dissolution of single NPs. Pan and coworkers used LSPR dark-field scattering to track the electrodeposition of single Ag NPs.[52] When the applied potential was scanned to negative values, LSPR scattering emerged and increased in intensity, which signified the formation and growth of NPs by reduction of Ag^+. The onset potential and growth kinetics were found to be variable from NP-to-NP (Figure 5b). The LSPR

scattering intensity was also used as a reporter of the NP size by using calibration information from correlated scanning electron microscopy (SEM) imaging. From the estimated NP size, the researchers determined the Faradaic current for Ag^+ reduction as a function of applied potential, thus allowing them to reconstruct single-NP-level voltammetric curves, not otherwise accessible by bulk-level electrochemistry. The reverse process of oxidative dissolution of Ag NPs was investigated by Willets and coworkers by a combination of dark-field microscopy and super-localization imaging.[53] Upon the application of a potential of 1.2 V, the LSPR scattering of individual Ag NPs decreased in intensity, indicating oxidative dissolution. By monitoring the time trajectory of this decrease (Figure 5d), the dissolution kinetics was determined for a number of single NPs. Consistent with Pan's study,[52] there was heterogeneity in the behavior of individual NPs ranging across fast oxidation, slow oxidation, and no oxidation. Super-localization of single NP scattering was performed to further characterize the heterogeneity. In cases of fast oxidation or no oxidation and some cases of slow oxidation, the spatial origin of the scattering did not change in the course of oxidation (Figure 5c, top). In other cases of slow oxidation, there was a marked shift in the location of scattering as oxidation proceeded (Figure 5c, bottom). The former type of spatial evolution of the scattering suggested symmetric oxidation of the NP, whereas the latter indicated asymmetric oxidation. There was yet another type of evolution which involved an abrupt jump in the origin of scattering when the potential was switched from 0 V to 1.2 V. The authors determined that the dissolution behavior depended on the presence of an oxide layer on the surface of the Ag NPs. In cases where an oxide layer was absent or thin, the dissolution was fast and took place uniformly. When a thick oxide layer was present on the surface, the dissolution was slow and asymmetric, if this layer was non-uniform. In a similar vein as the study of Willets and coworkers, LSPR scattering has been applied for understanding the manner of chemical etching of

NPs[54–57] and the formation of amalgams.[58,59] Tracking of nanometer-scale shifts in the scattering centroid of a single Au nanostructure has revealed the spatially inhomogeneous distribution of electrochemically-injected charge.[60,61] Together, these types of single-NP-level studies have advanced the understanding of mechanisms and of the effect of local environmental conditions on NP syntheses and NP transformations.

The use of light-absorbing NPs as heterogeneous photocatalysts for redox reactions is prominent and increasingly important. Huang and coworkers used LSPR scattering to monitor the photoinduced conversion of surface-bound 4-aminothiophenol (4-ATP) on plasmonic Ag NPs, to surface-bound *p,p*'-dimercaptobenzene (DMAB).[62] In the midst of a photoinduced reaction turnover, the LSPR spectrum of an individual Ag NP showed a relatively large initial red-shift followed by blue-shift of a smaller magnitude. From this sequence of LSPR shifts, a two-step reaction mechanism was inferred: 1) photoexcitation of a Ag NP in water generates energetic electrons that are transferred to dissolved O_2, forming a Ag^+/Ag_2O surface layer. The consequent reduction of electron density of the Ag NP and an increase in the surrounding refractive index due to the formation of the surface Ag_2O layer is manifested as the large LSPR red-shift; and 2) electron transfer from 4-APT to Ag^+ forms dimercaptobenzene and Ag_2O NPs at the Ag NP surface. The restoration of the electron density is seen as a blue-shift of the LSPR. However, the LSPR did not return to its original frequency because of a net conversion of Ag to Ag_2O, the formation of which leads to a higher local refractive index around the Ag NPs and a red-shifted steady-state LSPR. This work by Huang and coworkers demonstrates the power of single-NP LSPR scattering for resolving nanoscale details and elementary steps of chemical reactions.

3.2 Chemical reactions at or near the NP surface

In the previous subsection, we highlighted examples where the compositional or morphological sensitivity of the LSPR was exploited for monitoring solid-state or interfacial redox reactions at the single-NP level. In this subsection, we present case studies that demonstrate that the sensitivity of the LSPR to the refractive index of the surrounding medium can also be used for probing chemical reactions. It is known that the LSPR frequency decreases when the local refractive index of the NP increases. There is often an associated change in the peak LSPR intensity and a broadening of the LSPR peak. Thus, chemical reactions that induce a change in the refractive index within the near field of a NP can be detected in the form of changes in the LSPR scattering.[63–67] The LSPR response to a change in refractive index is an electrodynamic effect, but with appropriately engineered plasmonic nanostructures, it is highly sensitive.[68] In fact, refractive index sensing using LSPRs has even allowed the detection of the adsorption of a single molecule.[69] The LSPR of a plasmonic NP is altered not only by a change in the refractive index of the surrounding medium but also by coupling to a nearby electronic resonator, e.g., a chromophore or another plasmonic NP. In the examples we describe, a chemical event causes a change in the local refractive index or it introduces an electronic resonance near the NP, thereby allowing the chemical event to be detected by LSPR imaging and spectroscopy of single NPs. The spatial zone of LSPR sensitivity corresponds to the near-field of a plasmonic NP, which typically extends from a NP's surface out to a distance on the order of the dimension of the NP.[70,71] So, in addition to surface reactions, those occurring a few nanometers away from the surface can also be detected as well. The examples are categorized into chemical processes occurring at a NP surface and chemical reactions occurring in the near-field of a NP.

Surface reactions

Surface chemical processes such as adsorption-desorption are integral to the functionalization of NPs and engineering of NP properties. These processes are also invariably involved in the function of NPs as chemical and biological sensors, sorbents, and heterogeneous catalysts. In fact, the first and last steps in heterogeneous catalysis are surface adsorption and desorption. The

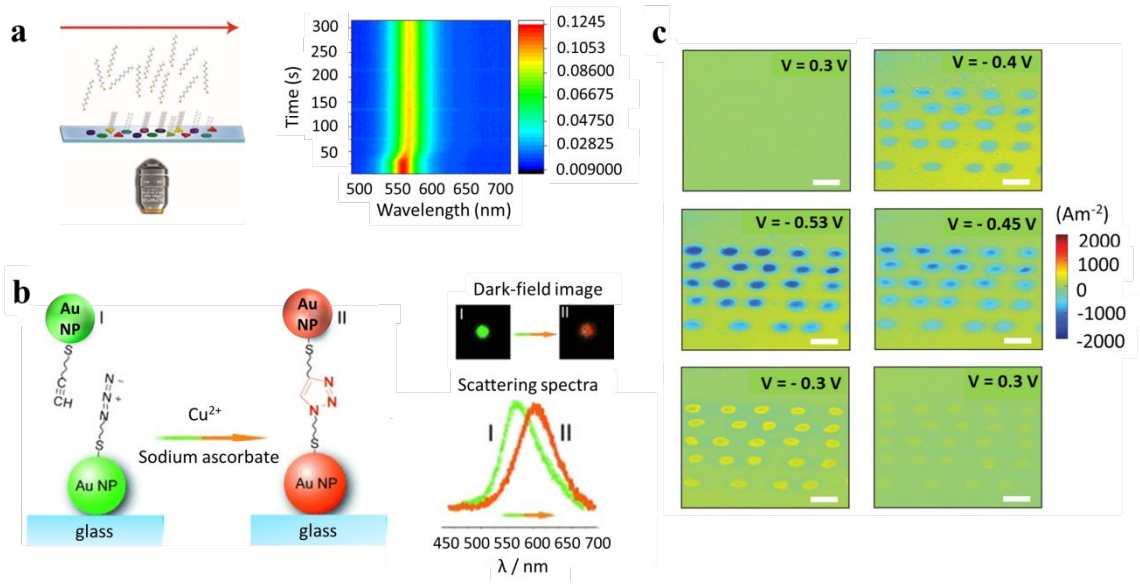

Figure 6. Single-NP level monitoring of surface chemistry studied using the refractive index sensitivity of LSPR scattering. (a) (Left) Schematic of an inverted dark-field microscopy configuration for monitoring the adsorption of alkanethiol molecules and SAM formation on individual Ag NPs. (Right) Color map showing the time-evolution of the dark-field scattering spectrum of a single Ag nanoparticle as a layer of alkanethiol molecules adsorbs and assembles on its surface. These processes increase the local refractive index of the NP and cause a red-shift in the LSPR frequency. The LSPR scattering intensity is represented by the color scheme provided in the legend. Reproduced from ref 72 with permission from the PCCP Owner Societies. (b) Strategy for reading out Cu^{+}-catalyzed azide-alkyne cycloaddition events at the single-NP level. Dark-field image and corresponding scattering spectrum of a Au NP before (I) and after (II) the click reaction. Formation of the triazole results in a linkage of NPs and a consequent coupling of their LSPRs, which is manifested as red-shift in the LSPR scattering spectrum. Reprinted with permission from ref 86. Copyright 2013 John Wiley and Sons. (c) SPR scattering images of microarrays of Pt NPs at various applied potentials serve as maps of the electrochemical current in the hydrogen evolution reaction. Spatially localized proton reduction results in a change in the local refractive index, which in turn causes a change in the SPR scattering intensity, from which the current is quantitatively estimated. While the example shown here is for microarrays of Pt NPs, the methodology was extended to the measurement of electrochemical currents on single Pt NPs. Scale bars have a 300 μm length. Reprinted with permission from ref 63. Copyright 2012 Springer Nature.

study of surface chemical processes is conventionally carried out on the bulk scale. Because of the structure sensitivity of these processes and the oft-present structural dissimilarities between individual grains of a catalyst, bulk-level measurements of rates and activation barriers average over a wide range of behaviors and activities, obscuring structure-activity relationships and mechanisms. By studying adsorption, desorption, and catalysis at the single-NP level, the mechanistic steps involved in these processes can be revealed and critical nanoscale features that influence reactivity, selectivity, and stability can be identified. This advance in understanding will be of utility for the rational engineering and design of surfaces, catalysts, and processes.

A more specific, but broadly implemented form of adsorption/desorption chemistry that is used for functionalization of nanomaterials is the formation of self-assembled monolayers (SAMs). Jain and coworkers applied single NP LSPR scattering microscopy for studying the initial stages of alkanethiol SAM formation on single Ag NPs.[72] The LSPR of single NPs red-shifted upon adsorption and SAM formation due to an increase in the local refractive index at the NP surface (Figure 6a). By tracking this frequency shift as a function of time, the kinetics of SAM formation on single NPs was followed. Single-NP trajectories showed an induction period, which was attributed to the time required for the setup of a thiol concentration field around a NP. The onset of adsorption was followed by gradual progress of adsorption and SAM formation over tens of seconds. The onset times and the time trajectories of growth were similar across the NPs, despite their heterogeneity. No sharp switch-like transformation was observed, quite unlike the single-NP-level kinetics of cation exchange and galvanic exchange reactions. These observations led to the inference that SAM formation was not limited by a critical step, rather it took place gradually by thiol molecules adsorbing randomly at sites across the entire NP. There was however a significant NP-to-NP heterogeneity in the rate of SAM formation and the final packing density of the SAMs

(as determined from the final LSPR frequency). From the distributions of rates across many individual NPs at different thiol concentrations, the authors inferred that there were two distinct modes for SAM growth. One mode, which dominates at lower concentrations, is via the migration of adsorbed thiols from the initial binding locations, which are the most active sites of the NP. This mode of growth leads to less variability in the SAM formation rate across the NPs and SAMs of higher quality. The other mode, which becomes operative at higher concentrations, is the direct adsorption of thiols from solution by replacement of pre-adsorbed solvent molecules or impurities present on the NP surface. When SAM formation takes place by both modes, the SAMs are more defective and the NPs exhibit significant heterogeneities in the SAM formation rate. The NPs exhibiting atypically high rates were likely ones with highly active facets and/or cleaner surfaces. Thus, single-NP studies in this case allowed resolution of the nanoscopic dynamics of SAM formation and elucidated how these dynamics affect the quality and variability of the surface passivating ligand layer.

The quality of surface functionalization also depends on the stability of the bond between the adsorbate and the NP surface. Huang and coworkers employed single-NP LSPR scattering for studying the stability of the bond between the surface of a Ag NP and the S atom of chemisorbed dithiocarbamate (DTC).[73] It was found that the bond is sensitive to visible light excitation. When visible light was used to excite the LSPR, energetic electrons were generated in the NP. The transfer of these electrons to DTC led to the breakage of the Ag-S bonds at the surface, which the authors were able to monitor in situ by LSPR scattering imaging and spectroscopy. Upon Ag-S bond cleavage, DTC decomposed to a sulfide species, the nature of which depends on the solution characteristics.[73,74] In a neutral pH environment, HS^- was the prevalent DTC decomposition product. The formed HS^- drove the sulfidation of the Ag surface to Ag_2S. Due to the higher

refractive index of Ag_2S, the sulfidation was manifested as a red-shift in the LSPR scattering frequency, a change in the scattering color of nanospheres from blue to yellow-green in dark-field images, and a decrease in the scattering intensity. By contrast, in acidic conditions, the DTC decomposition product was CS_2, which forms Ag_2S at a time-scale longer than that of the experimental measurement; therefore, no LSPR shift was observed. With such a strategy, the stabilities of metal-adsorbate bonds on plasmonic NP surfaces can be evaluated under a wide range of conditions including different pH, temperature, additives, chemical reactions, and light intensity.

Structural changes occurring in a molecular adsorbate layer at the surface of plasmonic NPs can also be probed by LSPR scattering, as elegantly showed by Long and coworkers, who monitored the reversible photoisomerization of azobenzene on single Au NPs.[65] The irradiation of azobenzene-labeled Au NPs with ultraviolet (UV) light resulted in the isomerization of the azobenzene to the *cis* form. This photoinduced change in the adsorbate layer was found to red-shift the LSPR spectrum of a Au NP, which was attributed to the higher surface crowding of the *cis* isomer, which effectively increases the local refractive index. Upon visible light irradiation, the *cis* isomer reverted to the *trans* isomer, which relaxes surface crowding and decreases the local refractive index; a blue-shift of the LSPR was consistently measured. The LSPR shift (6–7 nm in wavelength units) was found to be reversible over several UV-visible light excitation cycles.

In 2011, Alivisatos and coworkers employed LSPR spectroscopy of individual Au-Pd core-shell NPs for sensing the sorption of H_2 by Pd, an exceptional H_2 storage material.[75] In their study, the partial pressure of H_2 was modulated while the LSPR spectrum of individual NPs was continuously measured. As the partial pressure of H_2 was increased, the NP LSPR red-shifted, which indicated the uptake of H_2 by the Pd lattice. The formation of Pd hydride results in a change in the dielectric

function, effectively increasing the local refractive index experienced by the Au NP core (which is inert toward H_2) and causing the red-shift of the LSPR. As the partial pressure of H_2 was decreased, the LSPR blue-shifted, indicating the unloading of H_2 from the Pd shell. The trajectory of the LSPR frequency as a function of H_2 pressure varied considerably from NP to NP. These heterogeneities were traced to differences in the shape and Pd shell thickness of NPs. Furthermore, by spatial correlation of single-NP spectroscopy with SEM imaging, the authors found that decahedral NPs, which also happened to have thicker Pd shells, showed an initial blue-shift, instead of a red-shift, upon increase in the H_2 pressure. This blue-shift was caused by H_2 exposure-induced Au/Pd interdiffusion and formation of Pd silicide by the reaction of the NP with the silicon substrate. An ensemble-level study would not have revealed the atypical behavior of the decahedral shaped NPs. Such knowledge about the influence of NP shape on sorption activity can aid the improvement of NP-based sorbents, gas storage materials, and hydrogenation catalysts.

Not just NPs, but extended structures of noble metals, e.g., thin films, have also been used as platforms for nanoscale sensing of chemical reactions. Unlike zero-dimensional NPs, for thin films of noble metals, which are extended in two dimensions, the surface charge oscillation is not localized, but it propagates along the surface. This propagating charge oscillation mode is known simply as a surface plasmon resonance (SPR). But a free-space photon of the same frequency as a thin film SPR mode typically has a much smaller momentum. This momentum-mismatch prevents the direct excitation of an SPR by free-space light. Rather, incident light requires a coupler – such as nanostructured roughness or defects in the film, a grating, or a total internal reflection (TIR) excitation geometry – that increases the wavevector of light to match the SPR mode wavevector. In a TIR geometry, an SPR mode is most efficiently excited by light that is incident at an angle greater than the critical angle for TIR. The optimal angle of incidence is known as the SPR angle.

Similar to LSPRs, the SPR angle is sensitive to the refractive index of the environment of the metal film. Therefore, any change in the local refractive index caused by chemical processes will cause a change in the SPR angle, which is the principle behind SPR-based sensing. At a fixed angle of incidence, a change in the refractive index will cause a change in the scattering intensity from the region/s of the film where the change took place, which is the principle behind SPR microscopy. In pioneering work, Tao and coworkers combined SPR microscopy and electrochemistry for spatially resolved probing of electrochemical processes on plasmonic thin films[76,77] as well as on single NPs supported on thin films.[63,66,67,78] NPs in contact with a thin plasmonic film add contrast in the scattering image, which the researchers exploited for imaging microarrays of Pt NPs printed on a Au film. Furthermore, the catalytic activity of individual Pt NPs toward the H_2 evolution reaction was probed by monitoring changes in the SPR scattering in response to an applied potential under H^+ reduction conditions.[63] As the applied electrochemical potential was scanned to more negative values, the scattering contrast of individual Pt NPs increased due to a decrease in local refractive index resulting from the reduction of H^+ to form H_2 (Figure 6c). The researchers were also able to quantitatively estimate from the change in the SPR scattering signal the electrochemical current, a key metric of electrocatalytic activity, for each individual NP. Thus, by wide-field SPR imaging of individually resolvable NPs, high-throughput screening of NP electrocatalysts is possible. SPR microscopy has also been implemented for studies of nanoscale systems other than inorganic nanostructures, including nanobubbles[79] and biomacromolecules.[80]

Chemical processes occurring in the near-field

Noble metal NPs are being widely explored as electrocatalysts because of their electrical conductivities, high specific surface areas, and abilities to adsorb and activate small molecules. At

the same time, these NPs have strong visible-range LSPRs, which makes them ideal platforms for nanoscale studies of electrochemistry and electrocatalysis.[81,82] As one instructive example, Landes and coworkers tracked the LSPR spectra of individual Au NP monomers and dimers supported on a Au film and subjected to an applied potential under electrochemical reaction conditions.[83] The plasmon resonances of the NP and the film are coupled; this coupling leads to new hybridized plasmon modes. Electrochemically induced adsorption of sulfate anions on the Au surfaces led to a decrease in the conductivity of the underlying film, in turn influencing the coupled NP-film plasmon resonance modes. In particular, large red-shifts in the mode were observed. The measured changes in the single-NP LSPR scattering intensity, frequency, and linewidth as a function of the applied potential served effectively as a single-NP voltammogram from which the electrochemical activity at the NP could be characterized. Using this approach, the researchers detected and characterized the electroadsorption of perchlorate, acetate, and sulfate anions.[83]

LSPRs of two nearby NPs can couple leading to a hybridized plasmon resonance that is red-shifted with respect to the individual NP resonance. The magnitude of the spectral shift depends, among other factors, on the distance between the two NPs, a phenomenon that has been well characterized and implemented as a molecular ruler.[84,85] One of the first demonstrations of the use of LSPR coupling as a reporter of a chemical reaction was conducted by the Long group.[86] In this case, the well-known azide-alkyne click reaction catalyzed by Cu^{+} was detected. Two separate batches of Au NPs were prepared: one was surface functionalized with thiolated azide molecules and the other with thiolated alkyne molecules. Terminal azide-functionalized Au NPs were then immobilized on a glass substrate with an area density low enough for individual NPs to be resolved by dark-field LSPR scattering. Next, terminal alkyne-functionalized Au NPs and Cu^{+} (generated by the reaction of Cu^{2+} and sodium ascorbate) were introduced to this substrate, while the LSPR

images and spectra of immobilized NPs were monitored. When an azide-alkyne click reaction occurred it linked an alkyne-functionalized Au NP with the immobilized azide-functionalized NP. The resulting LSPR coupling was manifested as a change in the LSPR scattering color and a shift of the LSPR spectrum of the immobilized NP to the red (Figure 6b). Thus, the authors were able to monitor in real time the click reaction at the single-NP-level.

LSPR scattering imaging and spectroscopy offer label-free strategies for the detection and probing of chemical reactions on the nanoscale. In this section, we have documented numerous implementations of plasmonic metal NPs for chemical imaging. The large scattering cross-sections of plasmonic NPs make single-NP-level detection routine and allow high signal-to-noise measurements, ideal for detecting small, subtle changes occurring in interfacial and surface chemistry. However, the scattering cross-section falls off rapidly with a decrease in NP size, which typically disallows the implementation of LSPR-based methods for NPs with diameters smaller than ~30 nm.[42,87] There has been a recent advance in overcoming this challenge: by matching the refractive index of the collection objective to the specimen under study, it has been possible to increase the amount of collected light permitting dark-field scattering-based study of processes on NPs as small as 10–15 nm in diameter.[88] An additional limitation is that the phenomenon of LSPR is a very characteristic material property. Strong visible-range LSPRs are only exhibited by nanostructures of Ag and Au. Cu, which has similar LSPR properties, is prone to oxidation. As a result, the platforms that can be used for chemical studies are severely constrained to these two coinage metals. However, there are encouraging reports of dark-field Rayleigh scattering-based studies of chemical and electrochemical processes involving other materials such as cobalt NPs[89] and metal oxides.[53,90–92] Interferometric scattering[93] and reflectance[94,95] imaging offer other alternatives means for nanoscale studies of chemical and biological processes on non-plasmonic

nanostructures. There is one other limitation of LSPR scattering that must be pointed out: being a NP-scale property, LSPR scattering cannot typically provide intra-NP-level spatial resolution; it is not possible to resolve the reactivity of the distinct atomic sites that make up a NP.

4. Surface- and tip-enhanced Raman scattering

Plasmon-enhanced Raman scattering is an alternative approach for probing of chemical reactions with single-NP-scale spatial resolution and chemical specificity. Because Raman scattering spectra contain information about vibrational modes, they serve as chemically specific signatures for the detection and identification of species involved in a chemical process. No labels or *a priori* knowledge of the elementary steps of the chemical process are required. But Raman scattering has a cross-section that is too low for nanoscale detection. However, when molecules are in the near-field of optically excited plasmonic nanostructures, the Raman scattering cross-section is often enhanced by several orders of magnitude, allowing Raman scattering to be used for nanoscale detection and in some cases, even single-molecule-level detection in model systems.[96,97] In this section, we highlight two modes of plasmon-enhanced Raman scattering and their use for nanoscale chemical imaging and probing: surface-enhanced Raman scattering (SERS) and tip-enhanced Raman scattering (TERS). SERS requires a nanostructured surface (e.g., individual NPs or a film with nanoscale surface roughness) for enhancement of the Raman scattering of molecules present within the near-field. TERS utilizes a scanning probe microscopy (SPM) tip coated with a plasmonic material for local enhancement of the Raman scattering of molecules present between the tip and the substrate being imaged. Advantages and limitations of each approach are also described.

Surface-enhanced Raman scattering

Since its discovery in the late 1970s,[98,99] SERS has been recognized as a tool well-suited to the study of heterogeneous chemical reactions. Most early studies focused on ensemble-level measurements on electrochemically roughened surfaces, but over the past several decades the field of SERS has advanced. Chemical reactions are being probed at increasingly higher spatial and temporal resolution and sensitivities down to the single-NP and single-molecule levels. Here, we limit our discussion to implementations of SERS that go down to the single-NP and single-molecule levels, although advances have also been made in the time domain.[100] In a typical SERS measurement, a molecule of interest is adsorbed or allowed to adsorb onto the surface of a nanostructured plasmonic metal, typically Ag or Au. A laser is focused onto the surface so as to excite the metal-adsorbate complexes. The laser frequency is typically chosen to have overlap with the LSPR band of the nanostructures so that LSPRs are excited and large near-field intensities are sustained on the surface, a key requirement for plasmonic enhancement. Raman scattering is collected and detected with a CCD or photon counter. In some cases, a long focal length spectrometer placed in the detection path is used for obtaining a SERS spectrum rather than just an intensity signal. To reach the single-NP level, a dilute metal NP colloid is usually cast onto a transparent substrate with a low enough area density so that NPs can be individually resolved at typical optical microscopy magnifications. The metal colloid may be pre-coated with adsorbates or the adsorption may be performed after the deposition step. SERS at the single-molecule level is typically carried out by adsorbing a dilute concentration of probe molecules onto Ag or Au NPs in the colloidal state. Then, the colloid is aggregated using salt so that NPs form dimers of small NP clusters, which are then transferred onto a transparent substrate. Alternatively, such structures can be formed on the substrate by drying of the colloid. NP dimers and small NP clusters are known

to host strong electromagnetic field hotspots where Raman scattering can be enhanced by as much as 10 orders of magnitude.[101–104] Following this preparation procedure, SERS-active NP clusters are identified in an optical microscope by their strong Raman scattering under laser excitation. In the following subsection, we describe the use of SERS for nanoscale – ranging from single-NP to single-molecule-level – studies of photochemistry and electrochemistry in model chemical systems. We also highlight our laboratory's efforts to use SERS for obtaining nanoscale chemical insights into processes that go beyond model reaction systems.

Photochemistry

The most common model system for the study of a chemical reaction using nanoscale spatial resolution SERS is the light-induced reduction of 4-nitrothiophenol (4-NTP) on Ag nanostructured surfaces. In addition to providing the enhancement for Raman scattering, plasmon excitation of nanostructured Ag generates excited electrons that are thought to drive the reduction of adsorbed 4-NTP to 4-ATP or DMAB. A signature of reaction progress is a decrease in the intensity of the vibrational mode from the $-NO_2$ group of 4-NTP, along with an increase in the intensity of vibrational modes associated with the $-NH_2$ group of 4-ATP or the N=N bond in DMAB (Figure 7a,d). To study the light-induced conversion of 4-NTP to DMAB on the nanoscale with SERS, Wang and coworkers used 2 μm diameter Ag microparticles with nanoscale surface roughness (Figure 7b) as a photocatalyst and a SERS substrate.[105] The microparticles were coated with 4-NTP. Individual particles were isolated in an optical microscope, and excited with a continuous-wave 532 nm laser, which served as the light excitation source both for Raman scattering and for inducing the dimerization of 4-NTP to DMAB (Figure 7d). Changes in the SERS spectra occurring as a function of time were used to monitor the reaction progress. Using this method, the

photoreduction kinetics were measured at the single-particle level and the dependence of the kinetics on the excitation wavelength and intensity were also characterized. Wang and coworkers then obtained mechanistic insight into the interconversion of 4-ATP and DMAB by a

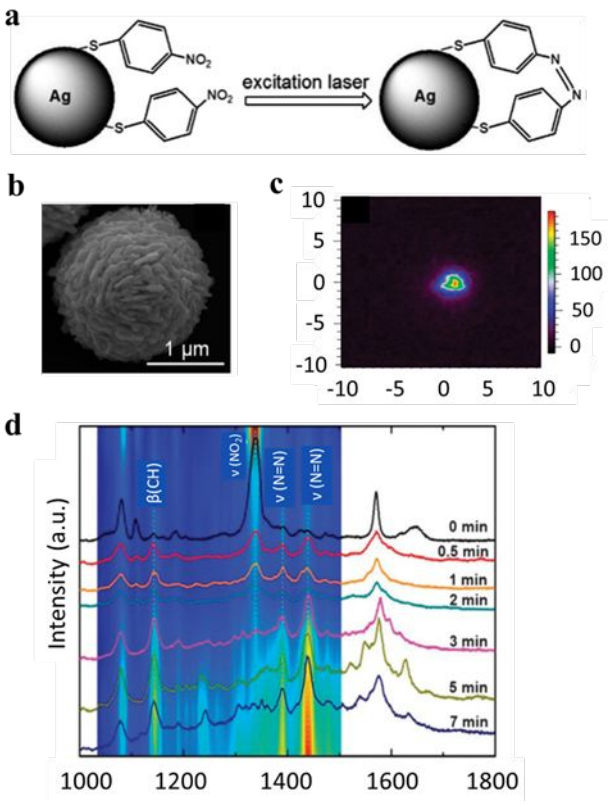

Figure 7. Single-particle-level monitoring of a photochemical reaction using SERS. (a) Scheme of plasmon-excitation-induced dimerization of surface-adsorbed 4-NTP to DMAB on a single Ag microparticle. (b) SEM image of a representative single Ag microparticle with nanoscale roughness used as a photocatalyst and a SERS substrate. (c) An (x,y) spatial image mapping the intensity of the 1335 cm^{-1} SERS peak corresponding to the $–NO_2$ group of 4-NTP at the start (t = 0 min) of the dimerization reaction induced by 532 nm laser excitation of the Ag microparticle. (x,y) axis labels are in units of μm. (d) Time-dependent SERS spectra from a 4-NTP-labeled Ag microparticle under continuous exposure of a 532 nm laser, which induces the dimerization reaction. The decrease in the intensity of the NO_2 vibrational mode along with the gradual increase in N=N vibrational mode as a function of time are used to track the progress of the light-induced dimerization reaction. Reproduced from ref 105 with permission from the Royal Society of Chemistry.

single-particle SERS study conducted under different controlled reaction environments.[106] It was found from the single-particle-level kinetics that in the presence of O_2 and water vapor, 4-ATP is

photoconverted to DMAB via a photothermally induced oxidation mechanism. On the other hand, in the presence of H_2O or H_2 as a $H\cdot$ source, but with O_2 absent, the DMAB is converted back to 4-ATP. The reverse reaction is thought to be mediated by plasmonically generated hot electron-driven reduction of the azo group of DMAB. A further follow-up single Ag particle-level SERS study showed that 4-NTP could be photoreduced by a two-step sequence via DMAB to 4-ATP light excitation under a H_2O or H_2 environment ideally with O_2 absent.[107] Additional SERS platforms that have been developed and used for the study of the photoconversions of 4-ATP and DMAB include Ag microflower NPs[108], NPs over a film,[109] Ag NPs coupled to Ag nanowires (which serve as waveguides for remote, polarized excitation),[110] and Ag microspheres coated with MoS_2 shells (which allowed a study of the effect of shell thickness and crystallinity).[111] These multifarious examples of SERS spectral monitoring of a model reaction demonstrate the unique power of vibrational spectroscopy for tracking the breaking and forming of chemical bonds on the nanoscale, a capability not inherently available with molecular fluorescence, NP PL, or LSPR scattering-based probing.

In the examples described above, the single-NP SERS measurement probed the conversion of many molecules adsorbed on a single NP surface. Deckert and coworkers asked whether the surface coverage of 4-NTP influences the photoinduced dimerization of 4-NTP to DMAB.[112] For this study, a colloid of Au NP dimers was mixed with a 4-NTP solution and the resulting complexes were dispersed on a glass substrate and individual dimers were identified in an optical microscope and subject to SERS study under laser excitation. A set of such experiments was conducted, with the concentration of 4-NTP varied over three orders of magnitude. With 4-NTP labeling concentrations of 10^{-7} M and 10^{-8} M, the photoconversion of 4-NTP to DMAB was observed to take place on a single dimer by SERS; a labeling concentration of 10^{-8} M required a higher laser

power to induce the reaction. With a 10^{-9} M labeling concentration, no formation of DMAB was observed. It was estimated that, at this low labeling concentration, the coverage of 4-NTP molecules on the Au surface is so sparse – the estimated inter-molecular spacing is ~32 nm – that the chance of dimerization is low. Instead of dimerization, the SERS spectra showed, that surface-adsorbed thiophenol was formed by the photoinduced dissociation of the $–NO_2$ group from a 4-NTP molecule. From the step-like decrease (increase) in the SERS intensity of the 1332 cm^{-1} (1017 cm^{-1}) mode of the 4-NTP (thiophenol), it was inferred that this conversion involves a solitary molecule of 4-NTP and no interactions between 4-NTP molecules, unlike in the photodimerization reaction, are involved. This example shows that inter- and intra-molecular chemical transformations can be distinguished by nanoscale resolution SERS.

One persistent challenge in the few-to-single molecule regime is that time-dependent changes in SERS spectra may reflect not only molecular transformations, but also physical dynamics (e.g., diffusion or rotation) of molecules. Weckhuysen and coworkers developed an analysis procedure to distinguish these two types of phenomena. Specifically, the researchers used a principle component analysis (PCA) followed by multivariate curve resolution (MCR) of SERS spectra collected in the process of photoreduction of 4-NTP on Ag NPs deposited on a flat Au surface.[113] PCA was first used to separate out the shorter timescale, reversible blinking fluctuations caused by physical dynamics from the longer timescale photoreaction dynamics of 4-NTP photodimerization. The longer timescale contribution thus obtained represents the pure reaction progress free of any spectral fluctuations. MCR analysis of this contribution by using two components (4-NTP and DMAB) yielded more reliable information about the reaction kinetics. MCA analysis of the short timescale contribution revealed four components, which may be assigned to transient events on the Ag surface, corresponding either to the reorientation of pNTP

or DMAB molecules, or to a reaction intermediate. Thus, this study shows that it may be possible to isolate and study transient intermediate or rare events that would otherwise be averaged out in larger ensemble and/or longer time-scale measurements.

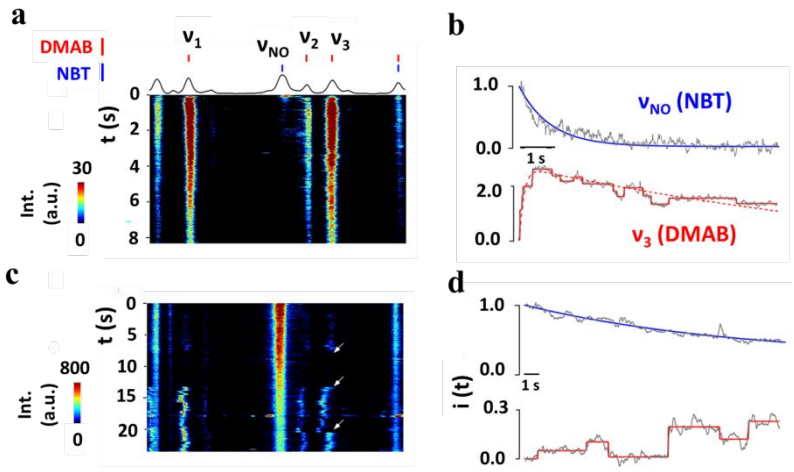

Figure 8. Single-molecule-level SERS monitoring of a photochemical reaction. Two examples of (a, c) a color map showing time-evolution of the SERS spectrum as 4-nitrobenzenethiol (NBT) undergoes photoinduced dimerization to DMAB at a Ag nanosphere–Au thin film junction. The SERS intensity is represented by the color scheme described in the legend. From the two color maps in (a, c), corresponding (b, d) time-trajectories of the SERS intensity of the ν_{NO} mode of NBT (blue) and the ν_3 mode of DMAB (red) were extracted, which are shown along with overlaid fits. The gradual decrease in the intensity of the ν_{NO} mode indicates that more than one molecule is present in the detected volume, whereas the discrete intensity jumps for the ν_3 mode indicate single DMAB formation events are being detected. (b). Reprinted with permission from ref 114. Copyright 2016 American Chemical Society.

Plasmonic NP aggregates are often used to generate electromagnetic enhancements that are large enough for the observation of single-molecule-level SERS. In such aggregates, the junction between the NPs concentrates incident light, creating localized areas with electric field intensities orders-of-magnitude higher than those on the surfaces of individual NPs. These junctions are therefore electromagnetic hot spots. However, the structural differences between individual NPs along with variations in aggregate geometry or the number of NPs in an aggregate result in significant heterogeneity in the field enhancement of hot spots. As a result, the SERS intensities

from individual hot spots are unpredictable and prone to orders-of-magnitude variations from one spot to another and fluctuations in time. To minimize hot spot heterogeneity in the single-molecule-level studies of 4-NTP photochemistry, Kim and coworkers used a geometry consisting of a 4-NTP monolayer sandwiched between Ag nanospheres and a Au film.[114] In this construct, the hot spots are localized at the junctions between the film and individual Ag nanosphere. The hot spots are thus relatively well-controlled; their SERS enhancement factors were within one order of magnitude of the predicted value and relatively steady in time. This allowed the researchers to use SERS spectra for tracking in real-time the single-molecule-level photodimerization of 4-NTP (Figure 8). In time-dependent SERS spectra from individual hot spots, the ν_{NO} vibration from 4-NTP was found to decrease in intensity gradually as it converted to either DMAB or to 4-ATP. Interestingly, at low 4-NTP coverages, discrete intensity jumps were observed in the ν_3 vibrational mode of DMAB, which indicated that single DMAB formation events were being detected (Figure 8). Analysis of the number, frequency, and magnitude of intensity jumps as a function of 4-NTP coverage, as well as a bianalyte analysis, supported the claim that the steps in the DMAB trajectories represent individual reaction events of two 4-NTP molecules dimerizing to a DMAB molecule. This study shows that the fabrication of well controlled SERS hotspots enables predictable SERS enhancement and minimizes random SERS time fluctuations, opening up the door to reliable chemical reaction imaging at the single-molecule level.[115]

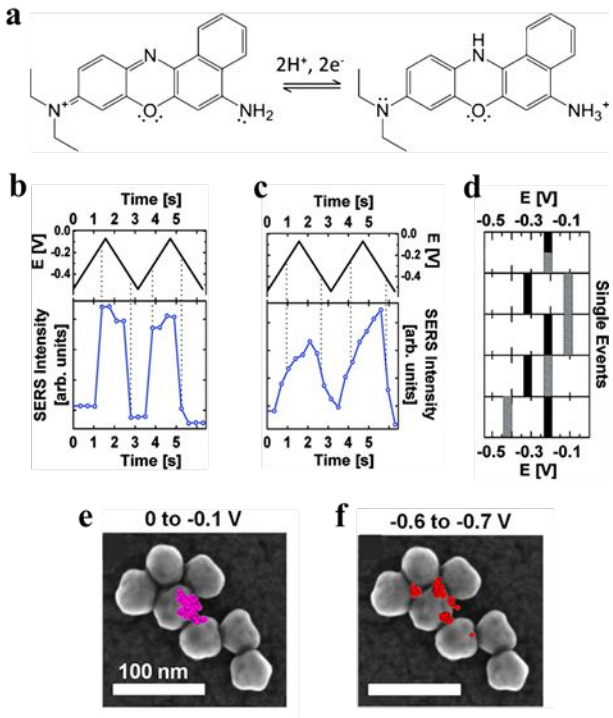

Figure 9. Single-to-few-molecule electrochemical events detected by SERS. (a) Mechanism of reversible reduction–oxidation of Nile Blue (NB) at pH = 6. The native oxidized form is a resonant, strong SERS emitter, whereas the reduced form is a non-resonant, weak SERS emitter, allowing reduction–oxidation events to be monitored by SERS. Reprinted with permission from ref 116. Copyright 2014 American Chemical Society. Change in the SERS intensity of the 590 cm^{-1} vibrational mode of NB under cyclic modulation of the electrochemical applied potential measured for (b) a single molecule and (c) many molecules. (d) Oxidation potentials measured from single-molecule reaction events. Each row represents a spatially unique single molecule and the black and grey bars correspond to oxidation potentials measured over two successive redox cycles. Reprinted with permission from ref 117. Copyright 2010 American Chemical Society. (x,y) map of the centroid positions of SERS emission from NB at (e) oxidizing and (f) reducing potentials, qualitatively overlaid on a SEM image of the underlying Au NP aggregate. The difference in the centroid positions under oxidation vs. reduction conditions indicates a site dependence of the electrochemical properties of NB. Reprinted with permission from ref 119. Copyright 2015 American Chemical Society.

Collectively, the examples highlighted in this subsection demonstrate that SERS can be used to monitor photochemistry at the single-NP and single-molecule levels through careful design of SERS substrates, systematic studies of analyte concentrations, and sophisticated data analyses. The 4-NTP–DMAB model system has paved the way for the use of SERS imaging and

spectroscopy for nanoscale studies of scientifically and technologically important chemical processes.

Electrochemistry

SERS has become particularly notable as a technique for probing chemistry at the single-NP and single-molecule levels in the field of electrochemistry. SERS studies of nanoscale electrochemistry often employ a molecular probe, the most common one being Nile Blue (NB), which undergoes a reversible multi-proton, multi-electron redox conversion (Figure 9a).[116] In its native oxidized form, NB is routinely detected by SERS at the single-molecule level because plasmonic enhancement is further supplemented by a visible-region electronic resonance of the NB. When NB is reduced, the molecular resonance is shifted to the UV region of the electromagnetic spectrum; the resonant enhancement of Raman scattering is no longer available and single molecules are no longer observable by SERS under visible light excitation. Thus, the appearance or disappearance of vibrational modes of NB in SERS spectra can be used as a reporter of electrochemical oxidation or reduction event, respectively. From studies of this model system, insights into NP-based electrodes and single-molecule electrochemistry have emerged.[116–121] In the following discussion, we highlight examples where new knowledge has been acquired by the optical tracking of electrochemistry at the nanoscale.

Etchegoin and coworkers first demonstrated the use of SERS for the study the electrochemistry of single molecules of NB adsorbed onto Ag NP aggregates.[117] By following the SERS intensity of a signature vibrational mode at 590 cm^{-1} as a function of potential, single-molecule electrochemical events were distinguished from multiple-molecule electrochemical events. Discrete, digital changes in the intensity were observed during electrochemical cycling, which

corresponded to the single-molecule reduction and oxidation events (Figure 9b). On the other hand, multiple-molecule redox events were manifested as a gradual rise or fall in the Raman mode intensity as a function of applied potential (Figure 9c). The potential at which oxidation occurred differed from one molecule to another. While some molecules showed reversible oxidation-reduction events, others showed irreversible behavior. Thirdly, the same molecule showed oxidation and reduction at different potentials in two successive voltammetric cycles (Figure 9d). These results indicate that the potentials at which molecules are reduced and oxidized are influenced by local electrochemical conditions (electrode and/or environment), which may themselves fluctuate in time. Using the same system, Cortés and coworkers analyzed the vibrational mode frequencies of single molecules and found them to be correlated with their electrochemical reactivity: molecules showing a higher frequency, i.e., a weaker interaction with the surface, got reduced at a much more negative potential.[118] Thus, it was found that the nature of the interaction of a molecule with the metal surface (including aspects such as the molecule-surface distance and orientation, presence of solvent molecules) influences the reduction and oxidation potential of single molecules. To resolve the sites of electrochemical activity on NP electrodes, Willets and coworkers used super-localization imaging of SERS emission originating from NB on Ag NP aggregates.[116] Their measurements revealed that the potential at which a molecule is oxidized or reduced depends on its position on the Ag NP aggregate. Spatial correlation of super-resolved SERS imaging and SEM images of the underlying NP electrodes showed that molecules residing in the NP junctions required the largest reduction overpotentials (Figures 9e and 9f).[119]

Van Duyne and coworkers extended single-molecule SERS studies of electrochemistry to Rhodamine 6G in an organic solvent and observed single one-electron transfer reduction events.[122]

Similar to the findings of Cortés and Willets,[116,118] a distribution of reduction potentials was observed and attributed to variations in the molecular orientation and the site of the electron transfer event. Sites on the Ag NP surface may differ from one another in their chemical potential, radius of curvature, and adsorption strength. The researchers also found that the distribution of reduction potentials measured by single-molecule SERS was broader than that measured by bulk electrochemistry, highlighting that the bulk measurement does not capture the full range of heterogeneity in environment experienced by individual molecules.

A more recent advance in SERS for nanoscale chemical imaging is the use of dual-wavelength probing, which can simultaneously monitor the reduced and oxidized forms of the probe molecules.[123] In this strategy, two excitation wavelengths are chosen, one with spectral overlap with a molecular resonance of the reduced form of the probe molecule, and the other with overlap with a molecular resonance of the oxidized form. This method is an advance over the on–off readout in the examples described above and it allows tracking of the structural dynamics of a molecule as it transitions between different oxidation states.

While some molecular-level insights into electrochemical processes have been obtained by SERS and other optical imaging/spectroscopy methods, thus far, these approaches have primarily complemented gains in knowledge brought about by techniques such as impact-based electrochemical detection of single NPs[124,125] and nanopipette[126] and nanoelectrode-based[127] electrochemistry, which have allowed studies of the kinetics of electrochemical reactions on individual NPs and molecules.

Beyond model reactions

The model photo- and electrochemical reactions discussed above have provided valuable insights, but they have mainly served as testbeds for establishing SERS as a tool for imaging

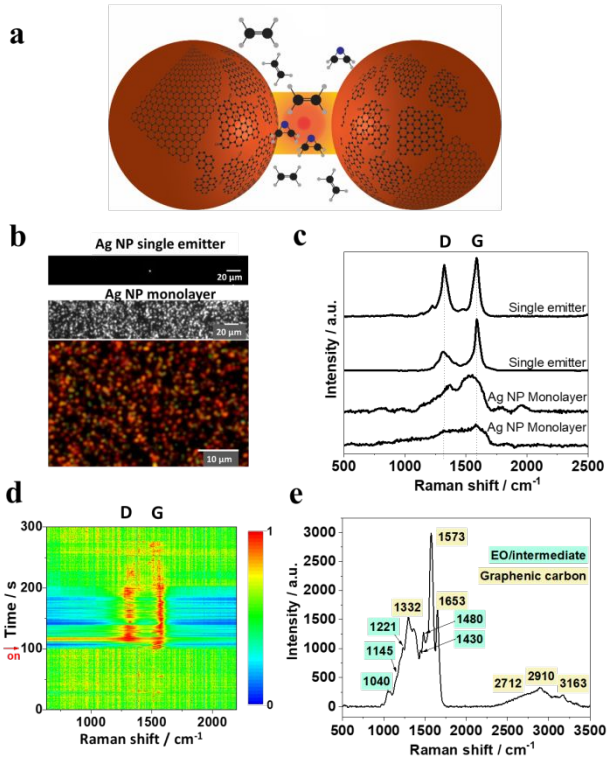

Figure 10. Single-NP-level SERS probing of the photocatalytic ethylene epoxidation reaction on Ag NPs. (a) A schematic showing the light-driven synthesis of graphenic carbon from ethylene on a Ag NP dimer. (b) Image of a spatially isolated SERS emission site under 514.5 nm laser excitation (top), a dark-field scattering image of a monolayer of Ag NPs excited by white light (middle), and a wide-field-view color image of dark-field scattering from a Ag NP monolayer (bottom). (c) SERS spectra obtained from a single emission site in the presence of ethylene and visible light exhibit well-defined graphenic carbon modes (labeled D and G modes) whereas those from a Ag NP monolayer show broad spectral features. (d) A color map showing the time-dependent SERS spectra from a single emission site, showing vibrational modes corresponding to graphene (D and G) and species associated with ethylene oxidation. The SERS intensity is represented by the color scale described in the legend. (e) A representative SERS spectrum from the time-stack of spectra is shown with major modes labeled and assigned to specific species. Reprinted with permission from ref 128. Copyright 2018 Springer Nature.

chemical reactions on the nanoscale, down to the single-NP and single-molecule levels. In this subsection, we will highlight recent advances from our laboratory that expand the scope of SERS-based nanoscale chemical imaging to industrially and technologically important reactions. Specifically, we describe nanoscale studies of photocatalytic ethylene epoxidation, CO_2 photoreduction, and water splitting by Photosystem II (PSII) all using Ag NPs as the SERS substrate. These examples showcase the application of nanoscale SERS beyond model reactions of a SERS tag or reporter such as Rhodamine 6G or 4-NTP. As a result, wide-scale nanoscale imaging in systems ranging from heterogeneous to homogeneous catalytic reactions is now possible.

Zhang et al. used SERS spectroscopy for the real-time probing of the plasmon-excitation-assisted ethylene epoxidation at ambient conditions catalyzed by Ag NPs (Figure 10).[128] SERS spectra were continuously acquired from Ag NPs in the presence of ethylene gas, air, and continuous excitation by a 514.5 nm laser, which served as the light source for both Raman scattering and the photoreaction. When the probing was performed on a monolayer of Ag NPs, broad spectral features were observed in the fingerprint region (Figure 10c), disallowing precise information about surface chemical events to be recovered. By contrast, new information emerged when the probing was carried out on individual diffraction-limited SERS emitters on a surface sparsely covered with Ag NPs (Figure 10b). The spectra were dynamic and showed well resolved modes that could be assigned to specific hydrocarbons formed by light-driven transformations of ethylene (Figure 10c). The spectra showed at early stages the formation of graphenic carbon on the Ag surface (Figures 10d, e). Under the photoreaction conditions, prior to the initiation of photo-epoxidation, ethylene undergoes condensation to graphene under the action of visible light and catalysis by the Ag surface (Figure 10a). The graphene nanofragments formed in situ then promote

the ethylene epoxidation reaction, as evidenced by the appearance of spectral modes of chemical intermediates and products of the reaction, which were assigned with the aid of density functional theory (DFT) calculations. Using the mechanistic insight, an improved photocatalyst consisting of a composite of graphene and Ag NPs was designed for ethylene epoxidation. Consistent with the predictions from nanoscale SERS imaging, the composite was found in bulk photocatalysis assays to be an order-of-magnitude more active toward ethylene photoepoxidation than unmodified Ag NPs. Our laboratory also found, as predicted by the time-evolution of SERS spectra, that unmodified Ag NP photocatalysts that were subjected to an atmosphere of ethylene and 514.5 nm light became considerably more active toward ethylene epoxidation. This activating effect was confirmed by SERS spectroscopy to be the result of in-situ photosynthesis of graphene on the Ag surface.

Recently, Kumari et al. used single-NP-level SERS to probe the plasmonic-excitation-induced CO_2 reduction reaction on Ag NP photocatalysts.[129] Under an atmosphere of CO_2 and humid air and continuous excitation by a 514.5 nm laser, spectra were acquired at 200 ms time resolution from single SERS emitters (typically Ag NP dimers) on a glass substrate sparsely covered with Ag NPs. Under these CO_2 photoreduction conditions, the SERS spectra from single emitters showed dynamic activity, varying from one spectrum to another. Analysis of spectra showed that the dynamic activity captured stochastic events of adsorbates (e.g., physisorbed CO_2) and common products of CO_2 reduction (such as CO and formic acid) forming on the Ag NP surface. Kumari et al. also detected in the spectra the formation of an *a priori* unexpected species, a surface-adsorbed hydrocarboxyl radical, HOCO*. This radical was determined with the aid of DFT calculations to be a critical intermediate in CO_2 photoreduction formed by the plasmon-excitation-

assisted transfer of one e^- and one H^+ to a physisorbed CO_2. This intermediate would have remained undetected in a bulk or ensemble-averaged kinetics study.

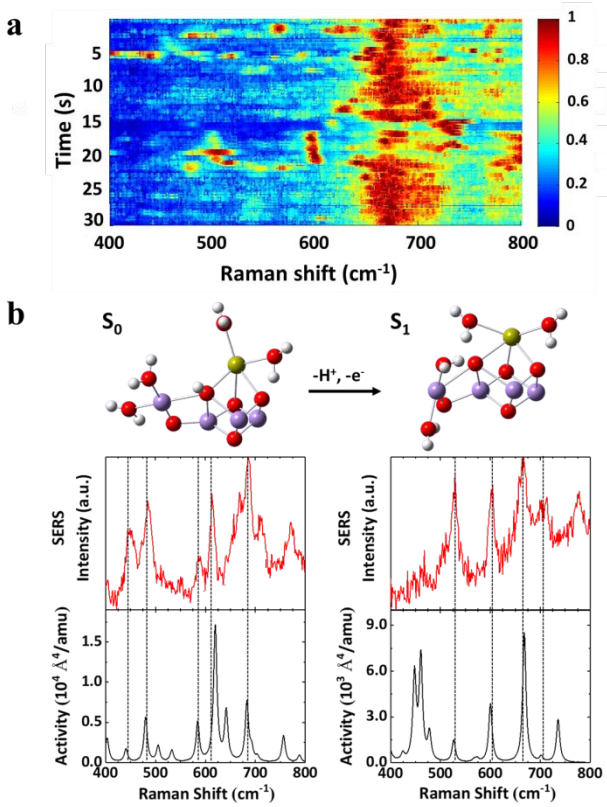

Figure 11. SERS-based nanoscale probing of water splitting by the oxygen-evolving complex (OEC) in Photosystem II (PSII). (a) Color map showing the time-evolution of the low-frequency region of SERS spectra of the Mn-oxo cubane OEC of PSII in water, which exhibits structural dynamics of the OEC during water splitting. The SERS intensity is represented by the color scheme provided in the legend. (b) Select intermediate structures (DFT-optimized geometries) in the catalytic cycle of the OEC in water splitting action captured in SERS spectra. Mn, O, H, and Ca atoms are represented by purple, red, white, and yellow spheres, respectively. Experimental spectra (red curves) are assigned to these specific intermediates by using Raman vibrational modes (vertical black lines) determined from spectra calculated by density functional theory (black curves). Reprinted with permission from ref 130. Copyright 2018 American Chemical Society.

The previous two studies provide a roadmap for label-free optical imaging of chemical reactions involved in heterogeneous catalysis and photocatalysis. Wilson and Jain further broadened the scope of nanoscale SERS imaging to the study of homogeneous catalysis. In this study, the low-

frequency region of SERS spectra was exploited for tracking the structural dynamics of the oxygen evolving complex (OEC) in Photosystem II (PSII) during a water splitting reaction (Figure 11).[130] Functional PSII was extracted from spinach and sparsely coated onto a film of Ag NPs. The resulting PSII clusters were active toward the water splitting reaction in the presence of water and green excitation light. Under these conditions, the Ag NPs served as electron sinks and plasmonically enhanced the Raman scattering from the overlaying PSII clusters, allowing SERS spectra to be acquired from individual PSII clusters in situ under water-splitting conditions. The OEC catalyst embedded within PSII contains Mn atoms that participate in low-frequency vibrational modes, which serve as reporters of catalytic activity. The low-frequency region of the spectrum is also relatively free of the myriad Raman scattering modes from the biological matrix, thus allowing selective monitoring of structural activity at the OEC catalytic sites. The SERS spectra acquired from sub-micron-size locations showed dynamic activity, which was assigned to the dynamics of OEC as it switches through different states in the catalytic water oxidation cycle. Transient intermediates of the OEC catalyst cycle were captured in several spectral snapshots (Figure 11b). These spectra, when aided by DFT calculations of Raman scattering modes, allowed our laboratory to assign the structures and protonation of the intermediate states in the catalytic cycle (Figure 11b). Such mechanistic information would not typically have been accessible in an ensemble-averaged measurement of PSII activity. This study also demonstrates the capability of SERS for probing solution-phase chemical reactions occurring in the near-field of a NP, which further extends the range of chemical processes that can be studied on the nanoscale.

Tip-enhanced Raman scattering (TERS)

SERS has been exploited for monitoring of chemical reactions at the single-NP and single-molecule levels by using sparse area densities of SERS emitters. Even then, the optical diffraction limit prevents the determination of the location of chemical activity with a precision better than ~250 nm. Nanometer-precision localization of chemical events is particularly desirable for resolving the chemical activity of individual atomic sites of a heterogeneous catalyst or surface. While super-resolution localization of SERS has been demonstrated,[7] it is not typically broadly applicable because it requires specialized conditions. A more general strategy for imaging chemical reactions with a resolution that surpasses the optical diffraction limit is to combine the chemical specificity and high sensitivity of SERS with the nanoscale spatial resolution of SPM. This strategy is termed as tip-enhanced Raman scattering (TERS). In a common TERS experiment, a nanosized SPM tip is coated with a plasmonic metal so that the tip has the dual capability of nanoscale mapping of topography and concentrating light for enhancement of Raman scattering. A laser is focused onto the plasmonic tip which is scanned over the surface of interest to generate a spatial map of the nanoscale topography of the surface co-localized with the plasmonically-enhanced Raman scattering from individual locations. The ultimate spatial resolution of this imaging is limited only by the diameter of the tip and is therefore on the order of 10 nm.[131] Further, because a plasmonic tip is used as a probe, TERS does not require a nanostructured, plasmonic substrate. Thus, quite unlike the case with SERS, it is possible to probe with sub-diffraction-limited spatial resolution chemical reactions occurring on non-plasmonic materials and surfaces of a wide range of roughness scales. Detection sensitivities down to the single-molecule level have been demonstrated.[132,133] For further details on the technical aspects and fundamentals of TERS, readers

are directed to recent reviews.[134–137] In this subsection we highlight seminal reports on the use of TERS for nanoscale imaging of chemical reactions on both bulk surfaces and single NPs.

Surfaces

Nearly contemporaneously, the Weckhuysen[138] and Xu[139] groups used TERS for nanometer scale imaging of the model photochemical conversion of 4-NTP to DMAB. Weckhuysen and coworkers used a Ag-coated atomic force microscopy (AFM) tip, which served as both the source of Raman enhancement and the photocatalyst for the dimerization of 4-NTP molecules immobilized in the form of a SAM on the surface of Au nanoplates (Figure 12a).[138] To separately resolve dynamics associated with physical and chemical processes, two excitation wavelengths were used. A green laser was used for photoexciting the Ag tip to induce the reaction. Following a short burst of low power that is enough to trigger the reaction, the green laser excitation was turned off and the reaction was monitored in time by measuring the Raman scattering excited by a red laser, which does not itself photoinduce the reaction. The vibrational mode signatures in the Raman spectra allowed the monitoring of the reaction occurring at the TERS tip (Figure 12b). In addition to the dimerization of 4-NTP, the researchers detected Raman scattering intensity fluctuations, which were assigned to dynamic changes in the SAM, which accompany the reaction. Using this strategy, the researchers demonstrated the dynamic imaging of photochemistry with a nanoscale spatial resolution, well-below the diffraction limit of visible light.

Xu and coworkers developed a high-vacuum system compatible with TERS and used it to study the dimerization of 4-NTP to DMAB.[139] The researchers used a Au scanning tunneling microscopy (STM) tip to image a Ag substrate coated with a SAM of 4-NTP molecules. The junction between the STM tip and substrate served to concentrate the excitation light resulting in amplification of the Raman scattering of molecules within the junction. The researchers exploited multiple

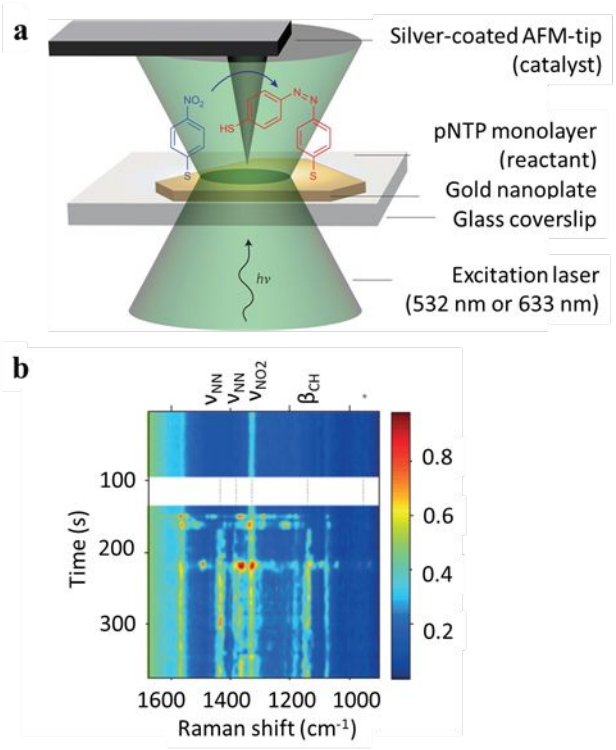

Figure 12. Nanoscale imaging of photochemistry on a surface by TERS. (a) Schematic of the experimental set up: The sample is mounted in an inverted optical microscope equipped with an AFM. TERS spectra are collected from a SAM of 4-NTP molecules localized at the junction between the Au nanoplate support and the Ag-coated AFM tip under continuous excitation by 532 nm (green) and 633 nm (red) lasers. (b) Color map showing the time-evolution of TERS spectra, which exhibit the reduction of 4-NTP to DMAB and structural changes in the SAM occurring at the apex of the AFM tip. The TERS intensity is represented by the color scheme provided in the legend. Reprinted with permission from ref 138. Copyright 2012 Springer Nature.

advantages of using a STM tip: the tunneling current, tip bias, and tip-substrate distance could be controlled. These parameters along with the light intensity affect the electromagnetic field in the gap and consequently influence the degree of 4-NTP photo-conversion. In addition, Xu and coworkers measured Stokes and anti-Stokes TERS spectra from which they extracted the local temperature under photoexcitation conditions. The temperature rise resulting from photothermal heating was found to be rather limited possibly due to the rapid propagation of heat away from the junction. This allowed the researchers to conclude that the photoconversion of 4-NTP is primarily

driven by hot electrons generated by plasmonic excitation and plasmonic heating does not appear to be responsible.[139,140] Sun and coworkers[141] further extended the use of high-vacuum TERS (HV-TERS) in a study where a photoexcited plasmonic STM tip was used to both induce and monitor the controlled fragmentation of a model dye, Malachite Green (MG), adsorbed on Au and Ag surfaces. NC_2H_6 fragments were dissociated from MG due to the resonant excitation of a specific bond in MG and further assisted by the injection of photogenerated hot electrons from the plasmonic STM tip into the MG. The researchers also demonstrated control of the rate of photodissociation through control of the laser intensity, tip current, and bias.

TERS studies of interfacial chemistry in ambient and high-vacuum conditions constitute an important first step in the successful bridging of sub-diffraction-limited spatial resolution and chemical specificity. However, many important processes in nature as well as in energy conversion and storage are critically dependent on chemical and electrochemical reactions occurring at solid-liquid interfaces. To investigate such chemistry on the nanoscale, the Ren[142] and Van Duyne[143] groups have pioneered the integration of TERS with electrochemical systems. Ren and coworkers insulated a Au STM tip, which they used for local probing of electrochemistry on a surface, with a thin layer of polyethylene glue so that the tip did not contribute to Faradaic current, but only served to enhance Raman scattering from molecules in the tip-surface gap.[142] Using this insulated STM tip, TERS spectra of ((4'-pyridin-4-yl)biphenyl-4-yl)methanethiol (4-PBT) adsorbed on a Au(111) single crystal electrode were measured as a function of an applied electrochemical potential. Potential-dependent changes in the spectral features were attributed to changes in the protonation state of 4-PBT molecules. Another interesting observation from control measurements was that potential-dependent TERS spectra of 4-PBT on Au(111) differed in their spectral features from potential-dependent SERS spectra of 4-PBT on Au NPs. This difference resulted from the

prevalence in the SERS geometry of double-end-bonded structures of 4-PBT molecules trapped in junctions of Au NP dimers. In the TERS geometry, the molecules are primarily single-end-bonded, which allows their potential-dependent protonation–deprotonation. This finding highlights the potential of novel insight arising from the use of TERS. In a slightly different approach, Van Duyne and coworkers used a Au coated AFM tip for a nanoscale study of the electrochemistry of NB adsorbed onto an ITO electrode.[143] By following the 591 cm^{-1} mode of NB in TERS spectra, the authors were able to monitor the redox conversions of NB under potential cycling. Voltammograms were constructed from the change in the intensity of the 591 cm^{-1} vibrational mode as a function of the applied potential. Local voltammograms measured by TERS showed step-like behavior, which indicated that the measurement was probing the redox electrochemistry of a single or a few molecules contained within the nanoscale volume sandwiched between the tip and the ITO substrate being probed. This nanoscale resolution measurement revealed that the coverage of NB was non-uniform across the surface. In this system, the electrochemical response of TERS spectra was found to be comparable to that of SERS spectra but it was shifted ca. 100 mV more negative as compared to conventional cyclic voltammetry measurements. This difference was attributed to the tip locally altering the effective potential experienced by NB molecules. In a follow-up study, local cyclic voltammograms of NB measured by TERS were fit to a Lavrion model for adsorption.[144] From this analysis, the formal potential was determined for molecules at many individual nanoscale locations on the ITO electrode. The formal reduction potential showed a significant variation across the interrogated locations. The variation was attributed to the structural heterogeneities of the polycrystalline ITO surface on which NB was adsorbed. The reduction potentials showed a greater degree of variation as compared to the

oxidation potentials, which led to the inference that the oxidized cationic form of NB was more sensitive to the local environment than the reduced neutral form of NB.

The use of TERS as a tool for nanoscale investigations of chemical reactions was recently expanded to bimetallic surfaces.[145] Bimetallic surfaces have been a subject of wide interest in catalysis because bimetallic compositions often exhibit unique, composition-dependent catalytic properties as compared to the component metals, but deciphering the precise role of each component metal, whether synergetic or individual, is often challenging due to nanoscale structural and compositional heterogeneities of bimetallic surfaces. Bulk-scale measurements average over these heterogeneities and obscure structure-activity or composition-activity relationships. Recent work by Ren and coworkers showcased the capability of TERS for nanoscale investigation of structure-activity relationships on bimetallic surfaces. The researchers used TERS to measure with a 3 nm spatial resolution the oxidation of phenyl isocyanide to phenyl isocyanate on a bimetallic Pd/Au(111) surface.[145] By exploitation of the sub-diffraction-limited spatial resolution, specific sites of the bimetallic substrate including step edges and terraces were distinguished and their individual catalytic activity was determined. The frequency of the vibrational mode of the N≡C moiety of phenyl isocyanide was found to be sensitive to the atomic geometry and electronic structure of the bimetallic surface: the frequency was lower at Pd step edges as compared to Pd terraces, indicating a weaker N≡C bond, which correlated with an enhanced reactivity of the isocyanide to isocyanate at step edges. Using TERS, the ensemble size can be considerably reduced, thus allowing access to much more precise information about the influence of surface composition and local environment on reactivity as compared to bulk-scale measurements.

Single NPs

The TERS studies described thus far were limited to surfaces. However, TERS can also be applied to the study of single NPs. Using TERS, Roy and coworkers mapped with 20 nm resolution

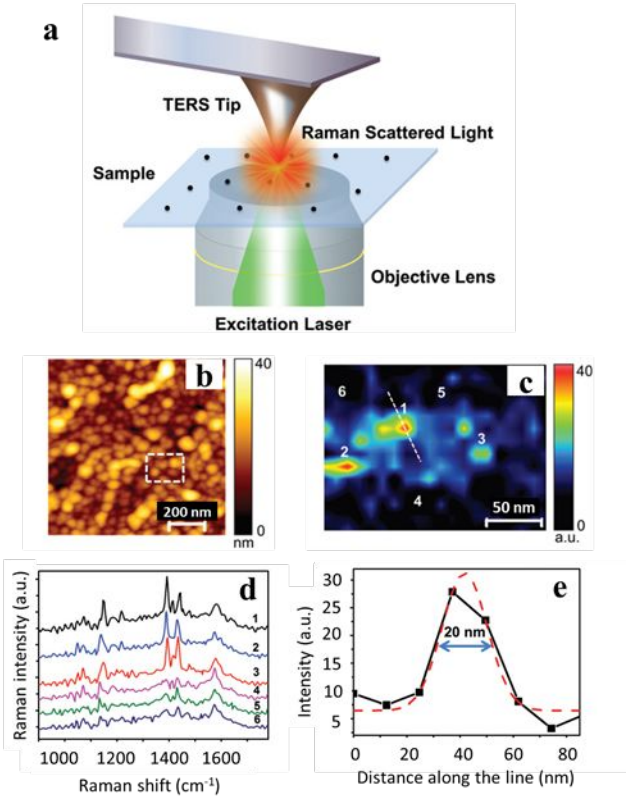

Figure 13. Imaging photochemistry at single NPs with TERS. (a) Schematic view of the experimental set up: An AFM tip is scanned over a film of Ag NPs functionalized with 4-NTP for nanoscale resolution mapping of both the topography and the photocatalytic activity. A focused laser photoexcites the NPs thereby driving the dimerization of adsorbed 4-NTP to DMAB. The laser also excites the AFM tip producing the field enhancement and allowing local TERS to be measured from the adsorbed molecules. (b) Spatial map of the topography of a thin film of Ag NPs on a glass substrate. (c) Spatial map of the TERS intensity of the 1142 cm^{-1} mode of DMAB over the area marked by a rectangle in (b). (d) TERS spectra from individual locations marked in (c) showing the location-to-location heterogeneity in the intensity of the vibrational modes of DMAB. (e) Profile of the TERS intensity of the 1142 cm^{-1} mode along the line shown in (c) showing a spatial resolution of 20 nm. Reproduced from ref 146 with permission from the Royal Society of Chemistry.

the photocatalytic activity of a film of Ag NPs toward the photoconversion of 4-NTP to DMAB (Figure 13a).[146] To accomplish this, a Ag AFM tip was coated with a thin layer of alumina so that the tip does not participate catalytically but it still serves to enhance the Raman scattering of molecules at the tip apex. The researchers spatially mapped the intensity of the key vibrational mode of DMAB. The map showed that the surface was heterogeneous in terms of its catalytic activity (Figure 13b-d). A cross-section of a catalytically active region of the map indicated that a spatial resolution as low as 20 nm was achieved (Figure 13e). Owing to this high spatial resolution, NPs of high and low photocatalytic activity could be distinguished in the spatial maps. This study highlights the use of TERS for determination of the chemical and catalytic properties of individual NPs. It also demonstrates a general strategy for precluding the contribution of the tip to chemical reactivity while maintaining its function, allowing the gathering of nanoscale resolution topographic and chemical information of adsorbates, intermediates, and products.

Considerable progress has been made in the exploitation of TERS as a tool for nanoscale investigations of chemistry over the past two decades, but the technique is not without some limitations. Reproducible production of TERS tips is a core challenge.[135] Small differences in tips cause variabilities in enhancement factors and polarization responses, which reduce the reproducibility and reliability of TERS probing. Even when a well-characterized tip is used, the tip geometry and composition can easily change over the course of sample scans, causing spurious changes in TERS spectra over the duration of an experiment. Further, TERS mapping is time-consuming and the enhancement factors are generally lower than with SERS. Single-molecule-level TERS has been demonstrated,[132,133] but only for model systems consisting of probe molecules with strong resonances. There is a strong need for development of tips that provide larger and more

reproducible enhancements factors. Such an advance will extend the use of TERS beyond model reactions into the domain of chemically and technologically interesting reactions.

5. Summary and Outlook

In this article, we have reviewed several classes of chemical reactions that can be optically monitored on the nanoscale without the use of fluorescent labels by using NP PL, LSPR scattering, or plasmon-enhanced Raman scattering. Nanoscale kinetic measurements made possible by these methods reduce the size of the spatial ensemble, which allows insights into chemical reactivity and molecular mechanisms that are otherwise unattainable with conventional, bulk-level measurements that average over a much larger ensemble. The nature of the chemical reaction under study will dictate the appropriate choice of the optical imaging modality. NP PL and LSPR scattering leverage the high luminosity of individual NPs and chemical dependence of the signal to report on chemical reactions occurring in nanoscale locations. SERS and TERS being vibrational spectroscopy probes directly report on bond breaking and formation events involved in chemical processes, with sub-diffraction-limited spatial resolution and sensitivities that approach the single-molecule limit.

The examples discussed in this article showcase the breadth and depth of new information and knowledge obtainable by nanoscale optical imaging of chemical reactions. Notwithstanding the advances made, there remain several limitations with these approaches. By overcoming these challenges, nanoscale optical imaging methods can become capable of providing in-depth holistic understanding of chemistry of any kind at the molecular level. One pressing issue is the need to concurrently reduce both the spatial and temporal sampling sizes, which would allow quantum events to be detected and understood. The temporal resolution in most experiments conducted thus

far have been limited by the electronic response of the instrumentation and the sensitivity of the probe. The temporal resolution currently achievable is on the order of several milliseconds to seconds. Electronic and vibrational transitions involved in chemical reactions occur many orders-of-magnitude faster. To address this challenge, the merger of ultrafast measurements with nanoscale SERS spectroscopy is underway.[100] Such a merger will allow us to build a space-time picture of molecular dynamics during a chemical reaction. Ultrafast probing on the nanoscale or single-molecule levels will lead to insights that are hidden by ensemble-averaging in conventional ultrafast measurements on heterogeneous systems. For LSPR- and PL-based probing of solid-state reactions, temporal super-resolution microscopy[147] could be a viable strategy for reducing temporal sampling size and reaching a microsecond time-resolution. Second, infrared spectroscopy should be exploited as a complement to Raman scattering,[137,148] especially in light of the recent progress in enhancing the sensitivity, which has allowed the detection of a small collection of molecules.[149,150] Nanoscale resolution surface-enhanced infrared spectroscopy would allow access to additional vibrational modes and provide a richer chemical picture of reactions. Lastly, the scope of materials amenable to nanoscale optical imaging needs to be expanded beyond semiconductor and plasmonic materials to polymers, oxides, ceramics, and glasses. Some progress toward this goal has been achieved by use of the shell-isolated nanoparticle-enhanced Raman scattering (SHINERS) technique pioneered by Tian and coworkers.[151] In SHINERS, the active material to be studied is supported on a plasmonic nanostructure spaced by a coated shell of an inert material that does not participate in chemistry but permits optical signal enhancements. This strategy has enabled vibrational probing of chemical processes on non-plasmonic surfaces and in a wider range of enivornments.[152–155] As the toolbox for high-resolution optical imaging grows, so

will our ability to unlock chemical mysteries and use chemical knowledge for the benefit of society.

Corresponding Author

*jain@illinois.edu

Author Contributions

The manuscript was written through contributions of all authors. All authors have given approval to the final version of the manuscript.

ACKNOWLEDGMENTS

P.K.J. acknowledges financial support from the Arnold and Mabel O. Beckman Foundation through a Young Investigator award. A.J.W. was supported in part by a Springborn Postdoctoral Fellowship. This work was funded in part (support for D. D.) by the National Science Foundation under grant no. NSF CHE-1455011.

REFERENCES

1 X. Luo, D. Tsai, M. Gu and M. Hong, *Chem. Soc. Rev.*, 2019, **48**, 2458–2494.
2 A. Nemati, Q. Wang, M. H. Hong and J. H. Teng, *Opto-Electron. Adv.*, 2018, **1**, 180009.
3 The Nobel Prize in Chemistry 2014 - Press Release. https://www.nobelprize.org/prizes/chemistry/2014/summary/ (accessed August 14, 2018) Nobel Media AB 2018.
4 J. B. Sambur and P. Chen, *Annu. Rev. Phys. Chem.*, 2014, **65**, 395–422.
5 K. Li, W. Qin, Y. Xu, T. Peng and D. Li, *Front. Optoelectron.*, 2015, **8**, 379–393.
6 T. Chen, B. Dong, K. Chen, F. Zhao, X. Cheng, C. Ma, S. Lee, P. Zhang, S. H. Kang, J. W. Ha, W. Xu and N. Fang, *Chem. Rev.*, 2017, **117**, 7510–7537.
7 K. A. Willets, A. J. Wilson, V. Sundaresan and P. B. Joshi, *Chem. Rev.*, 2017, **117**, 7538–7582.
8 W. Wang, *Chem. Soc. Rev.*, 2018, **47**, 2485–2508.
9 S. Dery, E. Amit and E. Gross, *Top. Catal.*, 2018, **61**, 923–939.
10 X. Mao, C. Liu, M. Hesari, N. Zou and P. Chen, *Nat. Chem.*, 2019, **11**, 687–694.
11 T. Jollans, M. D. Baaske and M. Orrit, *J. Phys. Chem. C*, 2019, **123**, 14107–14117.
12 C. L. Bentley, J. Edmondson, G. N. Meloni, D. Perry, V. Shkirskiy and P. R. Unwin, *Anal. Chem.*, 2019, **91**, 84–108.
13 S. Amemiya, A. J. Bard, F.-R. F. Fan, M. V. Mirkin and P. R. Unwin, *Annu. Rev. Anal. Chem.*, 2008, **1**, 95–131.
14 G. Wittstock, M. Burchardt, S. E. Pust, Y. Shen and C. Zhao, *Angew. Chem. Int. Ed.*, 2007, **46**, 1584–1617.
15 N. Ebejer, A. G. Güell, S. C. S. Lai, K. McKelvey, M. E. Snowden and P. R. Unwin, *Annu. Rev. Anal. Chem.*, 2013, **6**, 329–351.
16 A. Sakdinawat and D. Attwood, *Nat. Photonics*, 2010, **4**, 840.
17 Y.-S. Yu, M. Farmand, C. Kim, Y. Liu, C. P. Grey, F. C. Strobridge, T. Tyliszczak, R. Celestre, P. Denes, J. Joseph, H. Krishnan, F. R. N. C. Maia, A. L. D. Kilcoyne, S. Marchesini, T. P. C. Leite, T. Warwick, H. Padmore, J. Cabana and D. A. Shapiro, *Nat. Commun.*, 2018, **9**, 921.
18 H. A. Bechtel, E. A. Muller, R. L. Olmon, M. C. Martin and M. B. Raschke, *Proc. Natl. Acad. Sci.*, 2014, **111**, 7191.
19 C.-Y. Wu, W. J. Wolf, Y. Levartovsky, H. A. Bechtel, M. C. Martin, F. D. Toste and E. Gross, *Nature*, 2017, **541**, 511.
20 E. Kazuma, J. Jung, H. Ueba, M. Trenary and Y. Kim, *Science*, 2018, **360**, 521.
21 A. S. Kashin and V. P. Ananikov, *Nat. Rev. Chem.*, 2019, **3**, 624–637.
22 J. Wu, H. Shan, W. Chen, X. Gu, P. Tao, C. Song, W. Shang and T. Deng, *Adv. Mater.*, 2016, **28**, 9686–9712.
23 P. Frantsuzov, M. Kuno, B. Jankó and R. A. Marcus, *Nat. Phys.*, 2008, **4**, 519–522.
24 T. D. Krauss and J. J. Peterson, *J. Phys. Chem. Lett.*, 2010, **1**, 1377–1382.
25 L. Amirav and A. P. Alivisatos, *J. Am. Chem. Soc.*, 2013, **135**, 13049–13053.
26 J. B. Rivest and P. K. Jain, *Chem. Soc. Rev.*, 2013, **42**, 89–96.
27 A. L. Routzahn and P. K. Jain, *Nano Lett.*, 2014, **14**, 987–992.
28 S. L. White, J. G. Smith, M. Behl and P. K. Jain, *Nat. Commun.*, 2013, **4**, 2933.
29 A. L. Routzahn and P. K. Jain, *Nano Lett.*, 2015, **15**, 2504–2509.
30 A. Mooradian, *Phys. Rev. Lett.*, 1969, **22**, 185–187.

31 A. Tcherniak, S. Dominguez-Medina, W.-S. Chang, P. Swanglap, L. S. Slaughter, C. F. Landes and S. Link, *J. Phys. Chem. C*, 2011, **115**, 15938–15949.
32 Z. Zheng, T. Tachikawa and T. Majima, *J. Am. Chem. Soc.*, 2014, **136**, 6870–6873.
33 Z. Lou, M. Fujitsuka and T. Majima, *ACS Nano*, 2016, **10**, 6299–6305.
34 Y.-Y. Cai, J. G. Liu, L. J. Tauzin, D. Huang, E. Sung, H. Zhang, A. Joplin, W.-S. Chang, P. Nordlander and S. Link, *ACS Nano*, 2018, **12**, 976–985.
35 M. B. Mohamed, V. Volkov, S. Link and M. A. El-Sayed, *Chem. Phys. Lett.*, 2000, **317**, 517–523.
36 Z. Zheng, T. Tachikawa and T. Majima, *J. Am. Chem. Soc.*, 2015, **137**, 948–957.
37 Z. Zheng and T. Majima, *Angew. Chem. Int. Ed.*, 2016, **55**, 2879–2883.
38 Z. Lou, S. Kim, P. Zhang, X. Shi, M. Fujitsuka and T. Majima, *ACS Nano*, 2017, **11**, 968–974.
39 T. Tachikawa, I. Karimata and Y. Kobori, *J. Phys. Chem. Lett.*, 2015, **6**, 3195–3201.
40 T. Tachikawa, T. Ochi and Y. Kobori, *ACS Catal.*, 2016, **6**, 2250–2256.
41 C. Sönnichsen, T. Franzl, T. Wilk, G. von Plessen, J. Feldmann, O. Wilson and P. Mulvaney, *Phys. Rev. Lett.*, 2002, **88**, 077402.
42 P. K. Jain, K. S. Lee, I. H. El-Sayed and M. A. El-Sayed, *J. Phys. Chem. B*, 2006, **110**, 7238–7248.
43 J. G. Smith, Q. Yang and P. K. Jain, *Angew. Chem. Int. Ed.*, 2014, **53**, 2867–2872.
44 J. G. Smith and P. K. Jain, *J. Am. Chem. Soc.*, 2016, **138**, 6765–6773.
45 J. G. Smith, X. Zhang and P. K. Jain, *J. Mater. Chem. A*, 2017, **5**, 11940–11948.
46 Y. Park, C. Lee, S. Ryu and H. Song, *J. Phys. Chem. C*, 2015, **119**, 20125–20135.
47 S. Thota, Y. Zhou, S. Chen, S. Zou and J. Zhao, *Nanoscale*, 2017, **9**, 6128–6135.
48 J. G. Smith, I. Chakraborty and P. K. Jain, *Angew. Chem. Int. Ed.*, 2016, **55**, 9979–9983.
49 C. Novo, A. M. Funston and P. Mulvaney, *Nat. Nanotechnol.*, 2008, **3**, 598.
50 C. Novo, A. M. Funston, A. K. Gooding and P. Mulvaney, *J. Am. Chem. Soc.*, 2009, **131**, 14664–14666.
51 C. P. Byers, B. S. Hoener, W.-S. Chang, M. Yorulmaz, S. Link and C. F. Landes, *J. Phys. Chem. B*, 2014, **118**, 14047–14055.
52 C. M. Hill and S. Pan, *J. Am. Chem. Soc.*, 2013, **135**, 17250–17253.
53 V. Sundaresan, J. W. Monaghan and K. A. Willets, *J. Phys. Chem. C*, 2018, **122**, 3138–3145.
54 Y. Wang, H. Y. Zou and C. Z. Huang, *Nanoscale*, 2015, **7**, 15209–15213.
55 T. Xie, C. Jing, W. Ma, Z. Ding, A. J. Gross and Y.-T. Long, *Nanoscale*, 2015, **7**, 511–517.
56 S. Sun, M. Gao, G. Lei, H. Zou, J. Ma and C. Huang, *Nano Res.*, 2016, **9**, 1125–1134.
57 H. Z. Zhang, R. S. Li, P. F. Gao, N. Wang, G. Lei, C. Z. Huang and J. Wang, *Nanoscale*, 2017, **9**, 3568–3575.
58 Y. Liu and C. Z. Huang, *ACS Nano*, 2013, **7**, 11026–11034.
59 C. Schopf, A. Martin, M. Schmidt and D. Iacopino, *J. Mater. Chem. C*, 2015, **3**, 8865–8872.
60 T. Liu, S. Liu, W. Jiang and W. Wang, *ACS Nano*, 2019, **13**, 6279–6286.
61 K. A. Willets, *ACS Nano*, 2019, **13**, 6145–6150.
62 G. Lei, P. F. Gao, T. Yang, J. Zhou, H. Z. Zhang, S. S. Sun, M. X. Gao and C. Z. Huang, *ACS Nano*, 2017, **11**, 2085–2093.
63 X. Shan, I. Díez-Pérez, L. Wang, P. Wiktor, Y. Gu, L. Zhang, W. Wang, J. Lu, S. Wang, Q. Gong, J. Li and N. Tao, *Nat. Nanotechnol.*, 2012, **7**, 668.
64 C. Jing, F. J. Rawson, H. Zhou, X. Shi, W.-H. Li, D.-W. Li and Y.-T. Long, *Anal. Chem.*, 2014, **86**, 5513–5518.
65 H. Song, C. Jing, W. Ma, T. Xie and Y.-T. Long, *Chem. Commun.*, 2016, **52**, 2984–2987.

66 Y. Fang, H. Wang, H. Yu, X. Liu, W. Wang, H.-Y. Chen and N. J. Tao, *Acc. Chem. Res.*, 2016, **49**, 2614–2624.
67 Y. Wang, X. Shan, H. Wang, S. Wang and N. Tao, *J. Am. Chem. Soc.*, 2017, **139**, 1376–1379.
68 K. A. Willets and R. P. Van Duyne, *Annu. Rev. Phys. Chem.*, 2007, **58**, 267–297.
69 K. M. Mayer and J. H. Hafner, *Chem. Rev.*, 2011, **111**, 3828–3857.
70 P. K. Jain, W. Huang and M. A. El-Sayed, *Nano Lett.*, 2007, **7**, 2080–2088.
71 P. K. Jain and M. A. El-Sayed, *J. Phys. Chem. C*, 2007, **111**, 17451–17454.
72 J. G. Smith and P. K. Jain, *Phys. Chem. Chem. Phys.*, 2016, **18**, 23990–23997.
73 P. F. Gao, B. F. Yuan, M. X. Gao, R. S. Li, J. Ma, H. Y. Zou, Y. F. Li, M. Li and C. Z. Huang, *Sci. Rep.*, 2015, **5**, 15427.
74 G. Lei, P. F. Gao, H. Liu and C. Z. Huang, *Nanoscale*, 2015, **7**, 20709–20716.
75 M. L. Tang, N. Liu, J. A. Dionne and A. P. Alivisatos, *J. Am. Chem. Soc.*, 2011, **133**, 13220–13223.
76 K. J. Foley, X. Shan and N. J. Tao, *Anal. Chem.*, 2008, **80**, 5146–5151.
77 X. Shan, U. Patel, S. Wang, R. Iglesias and N. Tao, *Science*, 2010, **327**, 1363.
78 D. Jiang, Y. Jiang, Z. Li, T. Liu, X. Wo, Y. Fang, N. Tao, W. Wang and H.-Y. Chen, *J. Am. Chem. Soc.*, 2017, **139**, 186–192.
79 J. Chen, K. Zhou, Y. Wang, J. Gao, T. Yuan, J. Pang, S. Tang, H.-Y. Chen and W. Wang, *Proc. Natl. Acad. Sci.*, 2019, **116**, 12678.
80 M. Bocková, J. Slabý, T. Špringer and J. Homola, *Annu. Rev. Anal. Chem.*, 2019, **12**, 151–176.
81 A. J. Wilson, V. Mohan and P. K. Jain, *J. Phys. Chem. C*, 2019, **123**, 29360–29369.
82 B. S. Hoener, S. R. Kirchner, T. S. Heiderscheit, S. S. E. Collins, W.-S. Chang, S. Link and C. F. Landes, *Chem*, 2018, **4**, 1560–1585.
83 C. P. Byers, B. S. Hoener, W.-S. Chang, S. Link and C. F. Landes, *Nano Lett.*, 2016, **16**, 2314–2321.
84 C. Sönnichsen, B. M. Reinhard, J. Liphardt and A. P. Alivisatos, *Nat. Biotechnol.*, 2005, **23**, 741.
85 P. K. Jain, W. Huang and M. A. El-Sayed, *Nano Lett.*, 2007, **7**, 2080–2088.
86 L. Shi, C. Jing, W. Ma, D.-W. Li, J. E. Halls, F. Marken, Y.-T. Long, *Angew. Chem. Int. Ed.*, 2013, **52**, 6011–6014.
87 D. D. Evanoff and G. Chumanov, *J. Phys. Chem. B*, 2004, **108**, 13957–13962.
88 S. Hu, J. Yi, Y.-J. Zhang, K.-Q. Lin, B.-J. Liu, L. Chen, C. Zhan, Z.-C. Lei, J.-J. Sun, C. Zong, J.-F. Li and B. Ren, *Nat. Commun.*, 2020, **11**, 2518.
89 V. Brasiliense, J. Clausmeyer, P. Berto, G. Tessier, C. Combellas, W. Schuhmann and F. Kanoufi, *Anal. Chem.*, 2018, **90**, 7341–7348.
90 V. Brasiliense, J. Clausmeyer, A. L. Dauphin, J.-M. Noël, P. Berto, G. Tessier, W. Schuhmann and F. Kanoufi, *Angew. Chem. Int. Ed.*, 2017, **56**, 10598–10601.
91 K. Wonner, M. V. Evers and K. Tschulik, *J. Am. Chem. Soc.*, 2018, **140**, 12658–12661.
92 V. Sundaresan, J. W. Monaghan and K. A. Willets, *ChemElectroChem*, 2018, **5**, 3052–3058.
93 P. Kukura, H. Ewers, C. Müller, A. Renn, A. Helenius and V. Sandoghdar, *Nat. Methods*, 2009, **6**, 923–927.
94 D. Sevenler, O. Avci and M. S. Ünlü, *Biomed. Opt. Express*, 2017, **8**, 2976–2989.
95 J. F. Lemineur, J. M. Noël, D. Ausserré, C. Combellas and F. Kanoufi, *Angew. Chem. Int. Ed.,* 2018, **57**, 11998–12002.
96 S. Nie and S. R. Emory, *Science*, 1997, **275**, 1102.

97 K. Kneipp, Y. Wang, H. Kneipp, L. T. Perelman, I. Itzkan, R. R. Dasari and M. S. Feld, *Phys Rev Lett*, 1997, **78**, 1667–1670.
98 M. Fleischmann, P. J. Hendra and A. J. McQuillan, *Chem. Phys. Lett.*, 1974, **26**, 163–166.
99 D. L. Jeanmaire and R. P. Van Duyne, *J. Electroanal. Chem. Interfacial Electrochem.*, 1977, **84**, 1–20.
100 N. L. Gruenke, M. F. Cardinal, M. O. McAnally, R. R. Frontiera, G. C. Schatz and R. P. Van Duyne, *Chem. Soc. Rev.*, 2016, **45**, 2263–2290.
101 A. M. Michaels, M. Nirmal and L. E. Brus, *J. Am. Chem. Soc.*, 1999, **121**, 9932–9939.
102 A. M. Michaels, Jiang and L. Brus, *J. Phys. Chem. B*, 2000, **104**, 11965–11971.
103 Jiang, K. Bosnick, M. Maillard and L. Brus, *J. Phys. Chem. B*, 2003, **107**, 9964–9972.
104 J. P. Camden, J. A. Dieringer, Y. Wang, D. J. Masiello, L. D. Marks, G. C. Schatz and R. P. Van Duyne, *J. Am. Chem. Soc.*, 2008, **130**, 12616–12617.
105 L. Kang, P. Xu, B. Zhang, H. Tsai, X. Han and H.-L. Wang, *Chem. Commun.*, 2013, **49**, 3389–3391.
106 P. Xu, L. Kang, N. H. Mack, K. S. Schanze, X. Han and H.-L. Wang, *Sci. Rep.*, 2013, **3**, 2997.
107 L. Kang, X. Han, J. Chu, J. Xiong, X. He, H. Wang and P. Xu, *ChemCatChem*, 2015, **7**, 1004–1010.
108 X. Tang, W. Cai, L. Yang and J. Liu, *Nanoscale*, 2014, **6**, 8612–8616.
109 H. Wang, T. Liu, Y. Huang, Y. Fang, R. Liu, S. Wang, W. Wen and M. Sun, *Sci. Rep.*, 2014, **4**, 7087.
110 M. Sun, Y. Hou, Z. Li, L. Liu and H. Xu, *Plasmonics*, 2011, **6**, 681.
111 Y. Shen, P. Miao, C. Hu, J. Wu, M. Gao and P. Xu, *ChemCatChem*, 2018, **10**, 3520–3525.
112 Z. Zhang, T. Deckert-Gaudig, P. Singh and V. Deckert, *Chem. Commun.*, 2015, **51**, 3069–3072.
113 E. M. van Schrojenstein Lantman, P. de Peinder, A. J. G. Mank and B. M. Weckhuysen, *ChemPhysChem*, 2015, **16**, 489–489.
114 H.-K. Choi, W.-H. Park, C.-G. Park, H.-H. Shin, K. S. Lee and Z. H. Kim, *J. Am. Chem. Soc.*, 2016, **138**, 4673–4684.
115 H.-K. Choi, K. S. Lee, H.-H. Shin, J.-J. Koo, G. J. Yeon and Z. H. Kim, *Acc. Chem. Res.*, 2019, **52**, 3008–3017.
116 A. J. Wilson and K. A. Willets, *Nano Lett.*, 2014, **14**, 939–945.
117 E. Cortés, P. G. Etchegoin, E. C. Le Ru, A. Fainstein, M. E. Vela and R. C. Salvarezza, *J. Am. Chem. Soc.*, 2010, **132**, 18034–18037.
118 E. Cortés, P. G. Etchegoin, E. C. Le Ru, A. Fainstein, M. E. Vela and R. C. Salvarezza, *J. Am. Chem. Soc.*, 2013, **135**, 2809–2815.
119 M. L. Weber, A. J. Wilson and K. A. Willets, *J. Phys. Chem. C*, 2015, **119**, 18591–18601.
120 A. J. Wilson, N. Y. Molina and K. A. Willets, *J. Phys. Chem. C*, 2016, **120**, 21091–21098.
121 A. J. Wilson and K. A. Willets, *Analyst*, 2016, **141**, 5144–5151.
122 S. Zaleski, M. F. Cardinal, J. M. Klingsporn and R. P. Van Duyne, *J. Phys. Chem. C*, 2015, **119**, 28226–28234.
123 S. Zaleski, M. F. Cardinal, D. V. Chulhai, A. J. Wilson, K. A. Willets, L. Jensen and R. P. Van Duyne, *J. Phys. Chem. C*, 2016, **120**, 24982–24991.
124 Y.-G. Zhou, N. V. Rees and R. G. Compton, *Angew. Chem. Int. Ed.* 2011, **50**, 4219–4221. doi:10.1002/anie.20110088
125 X. Xiao and A. J. Bard, *J. Am. Chem. Soc.* 2007, **129**, 9610–9612.

126 K. McKelvey, S. R. German, Y. Zhang, H. S. White and M. A. Edwards, *Curr. Opin. Electrochem.*, 2017, **6**, 4–9.
127 S. G. Lemay, S. Kang, K. Mathwig and P. S. Singh, *Acc. Chem. Res.*, 2013, **46**, 369–377.
128 X. Zhang, G. Kumari, J. Heo and P. K. Jain, *Nat. Commun.*, 2018, **9**, 3056.
129 G. Kumari, X. Zhang, D. Devasia, J. Heo and P. K. Jain, *ACS Nano*, 2018, **12**, 8330–8340.
130 A. J. Wilson and P. K. Jain, *J. Am. Chem. Soc.*, 2018, **140**, 5853–5859.
131 Z. Yang, J. Aizpurua and H. Xu, *J. Raman Spectrosc.*, 2009, **40**, 1343–1348.
132 W. Zhang, B. S. Yeo, T. Schmid and R. Zenobi, *J. Phys. Chem. C*, 2007, **111**, 1733–1738.
133 M. D. Sonntag, J. M. Klingsporn, L. K. Garibay, J. M. Roberts, J. A. Dieringer, T. Seideman, K. A. Scheidt, L. Jensen, G. C. Schatz and R. P. Van Duyne, *J. Phys. Chem. C*, 2012, **116**, 478–483.
134 P. Verma, *Chem. Rev.*, 2017, **117**, 6447–6466.
135 X. Wang, S.-C. Huang, T.-X. Huang, H.-S. Su, J.-H. Zhong, Z.-C. Zeng, M.-H. Li and B. Ren, *Chem. Soc. Rev.*, 2017, **46**, 4020–4041.
136 N. Kumar, S. Mignuzzi, W. Su and D. Roy, *EPJ Tech. Instrum.*, 2015, **2**, 9.
137 D. Kurouski, A. Dazzi, R. Zenobi and A. Centrone, *Chem. Soc. Rev.*, 2020, **49,** 3315-3347.
138 E. M. van Schrojenstein Lantman, T. Deckert-Gaudig, A. J. G. Mank, V. Deckert and B. M. Weckhuysen, *Nat. Nanotechnol.*, 2012, **7**, 583.
139 M. Sun, Z. Zhang, H. Zheng and H. Xu, *Sci. Rep.*, 2012, **2**, 647.
140 Z. Zhang, L. Chen, M. Sun, P. Ruan, H. Zheng and H. Xu, *Nanoscale*, 2013, **5**, 3249–3252.
141 Z. Zhang, S. Sheng, H. Zheng, H. Xu and M. Sun, *Nanoscale*, 2014, **6**, 4903–4908.
142 Z.-C. Zeng, S.-C. Huang, D.-Y. Wu, L.-Y. Meng, M.-H. Li, T.-X. Huang, J.-H. Zhong, X. Wang, Z.-L. Yang and B. Ren, *J. Am. Chem. Soc.*, 2015, **137**, 11928–11931.
143 D. Kurouski, M. Mattei and R. P. Van Duyne, *Nano Lett.*, 2015, **15**, 7956–7962.
144 M. Mattei, G. Kang, G. Goubert, D. V. Chulhai, G. C. Schatz, L. Jensen and R. P. Van Duyne, *Nano Lett.*, 2017, **17**, 590–596.
145 J.-H. Zhong, X. Jin, L. Meng, X. Wang, H.-S. Su, Z.-L. Yang, C. T. Williams and B. Ren, *Nat. Nanotechnol.*, 2016, **12**, 132.
146 N. Kumar, B. Stephanidis, R. Zenobi, A. J. Wain and D. Roy, *Nanoscale*, 2015, **7**, 7133–7137.
147 W. Wang, H. Shen, B. Shuang, B. S. Hoener, L. J. Tauzin, N. A. Moringo, K. F. Kelly and C. F. Landes, *J. Phys. Chem. Lett.*, 2016, **7**, 4524–4529.
148 N. Heidary, K. H. Ly and N. Kornienko, *Nano Lett.*, 2019, **19**, 4817–4826.
149 L. Dong, X. Yang, C. Zhang, B. Cerjan, L. Zhou, M. L. Tseng, Y. Zhang, A. Alabastri, P. Nordlander and N. J. Halas, *Nano Lett.*, 2017, **17**, 5768–5774.
150 F. Neubrech, C. Huck, K. Weber, A. Pucci and H. Giessen, *Chem. Rev.*, 2017, **117**, 5110–5145.
151 J. F. Li, Y. F. Huang, Y. Ding, Z. L. Yang, S. B. Li, X. S. Zhou, F. R. Fan, W. Zhang, Z. Y. Zhou, D. Y. Wu, B. Ren, Z. L. Wang and Z. Q. Tian, *Nature*, 2010, **464**, 392.
152 N. Kumar, C. S. Wondergem, A. J. Wain and B. M. Weckhuysen, *J. Phys. Chem. Lett.*, 2019, **10**, 1669–1675.
153 C. S. Wondergem, T. Hartman and B. M. Weckhuysen, *ACS Catal.*, 2019, **9**, 10794–10802.
154 C.-Y. Li, J.-B. Le, Y.-H. Wang, S. Chen, Z.-L. Yang, J.-F. Li, J. Cheng and Z.-Q. Tian, *Nat. Mater.*, 2019, **18**, 697–701.
155 H. Zhang, C. Wang, H.-L. Sun, G. Fu, S. Chen, Y.-J. Zhang, B.-H. Chen, J. R. Anema, Z.-L. Yang, J.-F. Li and Z.-Q. Tian, *Nat. Commun.*, 2017, **8**, 15447.

Table of contents (TOC) graphic:

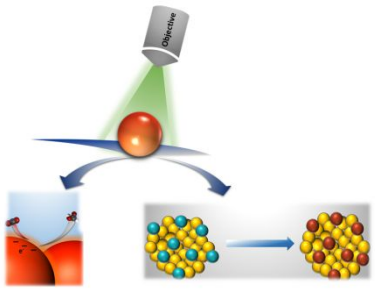

New advances in label-free optical imaging methods are allowing a wide range of chemical processes in surface science, catalysis, and photochemistry to be probed on the nanoscale and single-molecule levels.